UNIVERSIDAD NACIONAL AUTÓNOMA DE MÉXICO

FACULTAD DE INGENIERÍA

Experimental determination of constitutive behavior and reservoir compressibility

TESIS

Que para obtener el título de

Ingeniero Petrolero

P R E S E N T A

Cesar Yael Palacios Moyotl

DIRECTOR DE TESIS

Dr. Daniel Cabrera Sotelo

Ciudad Universitaria, Cd. Mx., 2025

PROTESTA UNIVERSITARIA DE INTEGRIDAD Y HONESTIDAD ACADÉMICA Y PROFESIONAL
(Titulación con trabajo escrito)

De conformidad con lo dispuesto en los artículos 87, fracción V, del Estatuto General, 68, primer párrafo, del Reglamento General de Estudios Universitarios y 26, fracción I, y 35 del Reglamento General de Exámenes, me comprometo en todo tiempo a honrar a la institución y a cumplir con los principios establecidos en el Código de Ética de la Universidad Nacional Autónoma de México, especialmente con los de integridad y honestidad académica.

De acuerdo con lo anterior, manifiesto que el trabajo escrito titulado EXPERIMENTAL DETERMINATION OF CONSTITUTIVE BEHAVIOR AND RESERVOIR COMPRESSIBILITY que presenté para obtener el titulo de INGENIERO PETROLERO es original, de mi autoría y lo realicé con el rigor metodológico exigido por mi Entidad Académica, citando las fuentes de ideas, textos, imágenes, gráficos u otro tipo de obras empleadas para su desarrollo.

En consecuencia, acepto que la falta de cumplimiento de las disposiciones reglamentarias y normativas de la Universidad, en particular las ya referidas en el Código de Ética, llevará a la nulidad de los actos de carácter académico administrativo del proceso de titulación.

CESAR YAEL PALACIOS MOYOTL
Número de cuenta: 317248951

RESUMEN

Este trabajo presenta una metodología que conjunta las técnicas de petrofísica experimental y la geomecánica, con el objetivo de estudiar la relación entre el comportamiento constitutivo y las propiedades petrofísicas de muestras de diámetro completo (núcleos) de arenisca bajo condiciones típicas de un yacimiento, es decir, presiones cercanas a las 12,000 psi y temperaturas promedio de 150 $°C$.

El enfoque distintivo de esta metodología radica en combinar condiciones de operación significativas para el yacimiento con el uso de muestras de diámetros completos, lo cual es poco común en la literatura actual. La mayoría de los estudios previos, realizados principalmente por empresas transnacionales, están orientados en estimar propiedades particulares a condiciones de esfuerzo y temperatura limitadas, que resultan poco representativas para cualquier clase de yacimiento.

Durante esta investigación se propone una metodología experimental que busca medir cuantitativamente la compresibilidad del yacimiento, lo que permite desarrollar correlaciones capaces de describir su interacción con otras variables, tales como la porosidad y permeabilidad; además, se ofrece un análisis más detallado sobre el comportamiento constitutivo de las muestras utilizadas, así como de su respuesta mecánica ante esfuerzos mediante la estimación de módulos elásticos.

En el capítulo 1 se abordan las bases de la investigación al presentar una detallada introducción sobre la importancia de la compresibilidad, su interacción con temas de producción, desarrollo y explotación de campos petroleros e inclusive su relación con temas políticos y sociales. Posterior a ello se muestran las directrices primarias de la investigación, así como los resultados a los que se pretenden llegar.

El capítulo 2 se centra en el estado de arte sobre la compresibilidad, así como de algunas variables relacionadas, con el fin de facilitar su entendimiento, incluyendo, además, la literatura correspondiente que le da soporte teórico a este trabajo.

Para el capítulo 3 se describe con detalle la forma de operar experimentalmente, la metodología empleada, así como figuras que muestran los procesos llevados a cabo. De igual forma se presentan los resultados, como los valores de la compresibilidad, porosidad y permeabilidad para ambas muestras, su interacción con el esfuerzo efectivo y tablas que contienen los datos reportados.

En el capítulo 4 se analizan las tendencias generadas de los datos experimentales y se desarrollan correlaciones entre la compresibilidad y las propiedades estudiadas, de esta forma se obtienen relaciones matemáticas que reflejan adecuadamente el comportamiento descrito.

En el capítulo 5 se estudia y explora el comportamiento mecánico de las muestras en función de los resultados experimentales, permitiendo desarrollar modelos analíticos que describan la respuesta mecánica de las muestras frente a estímulos de diferente orden. Además, es posible estimar valores confiables de los módulos elásticos derivados de los datos registrado, demostrando el acoplamiento exitoso entre la petrofísica y geomecánica.

Finalmente, el trabajo concluye en el capítulo 6, donde se discuten los resultados, limitaciones encontradas, así como recomendaciones para mejorar el experimento.

ABSTRACT

This work presents a methodology that integrates experimental petrophysics and geomechanics. The relationship between the constitutive behavior and petrophysical properties of full-diameter sandstone core samples were studied under reservoir conditions, specifically, high pressures and high temperatures. It is worth noting that studies using this approach are scarce, if not nonexistent, with most conducted by transnational companies. These studies typically estimate specific properties under limited stress and temperature conditions that poorly represent actual reservoir conditions.

This research proposes an experimental methodology designed to quantitatively measure reservoir compressibility, enabling the development of correlations that describe its interaction with other variables, such as porosity and permeability. Additionally, it provides a detailed analysis of the constitutive behavior of the samples used and their mechanical response to stresses through the estimation of elastic modulus.

Chapter 1 establishes the foundation of this research by providing a comprehensive introduction to the importance of compressibility, its relationship with oilfield production and development, as well as its connections to political and social aspects. Following this, the main research objectives and expected outcomes are presented.

Chapter 2 focuses on the state of the art related to the research topic, covering key concepts. It also presents relevant literature that established the theoretical foundation for this work.

Chapter 3 details the experimental procedures and methodology. It also presents the results obtained, including compressibility, porosity, and permeability values for both samples, their dependence of the effective stress, as well as tables containing the reported data.

Chapter 4 presents the analysis of trends observed in the experimental data and correlations derived from compressibility and the estimated properties. This process yielded mathematical relationships that accurately described the rock behavior.

Chapter 5 provides the samples' mechanical behavior based on experimental data obtained in earlier stages. This process facilitated the development of analytical models that describe the samples' mechanical response to the application of variable stress. Additionally, reliable estimates of elastic moduli were derived from the measured properties, demonstrating the successful integration of petrophysics and geomechanics.

Finally, the work concludes with Chapter 6, which discusses the results, certain limitations and provides recommendations for improving the experiment.

Agradecimientos

Este trabajo nació del cariño, esfuerzo y dedicación que me alentaron a superar cada desafío que se me presentó a lo largo de este recorrido. Nada de esto hubiera sido posible sin el apoyo de todas aquellas personas que creyeron en mí y caminaron a mi lado; a todas ellas les expreso mi más sincero agradecimiento. En este viaje entendí que no siempre se trata de ganar o perder, sino de vivir con pasión, con deseo, y con la firme intención de hacer de nuestra vida una pequeña obra de arte. Y en ese espíritu, he vivido y trabajado este proyecto.

A mis padres:

Los pilares que sostienen mi vida, apostando todo por mí aun cuando la incertidumbre era gigante. Esta hazaña ya no es solo mía, sino también suya. No sería el hombre que soy ahora sin su sabiduría ni su amor incondicional. Cada sacrificio, cada lagrima, cada abrazo en los momentos de duda quedan marcados en estas páginas. Gracias, mamá, papá, a mis hermanos, Edwin y Mariel, y a mi abuelita, Ani, por ser la fuerza en este sueño.

Al Dr. Daniel Cabrera, mi tutor:

Expreso mi más sincero reconocimiento por su invaluable guía, apoyo y confianza en el desarrollo de este proyecto, en el cual su huella queda profundamente plasmada. Su experiencia y compromiso fueron los cimientos para la culminación de este logro en mi vida. Su mentoría trascendió lo académico; fue una lección de vida y profesionalismo. Le estoy profundamente agradecido a usted y al laboratorio, y espero algún día poder retribuirle todo lo que me ha brindado. Gracias, Doctor.

Al ingeniero Jesús Zúñiga:

Por enseñarme, con su ejemplo, el valor de la paciencia y el verdadero compañerismo. Mi estadía en el laboratorio no hubiera sido la misma sin usted ahí. De usted aprendí que, en la teoría, la práctica es otra, y sin su ayuda, esto no hubiera sido posible.

A Ham:

Por demostrarme lo que es la lealtad, el apoyo, y la reciprocidad. Esta etapa coincidió con tu llegada, y ahora que se acerca su fin, solo puedo expresarte mi gratitud por cada momento compartido. Eres la inspiración que me alienta a seguir enfrentando nuevos desafíos, con la ilusión de que juntos celebremos cada logro que esté por venir.

A mis amigos:

Por aligerar con su humor, comprensión y apoyo el recorrido de este camino. Su amistad fue mi refugio. A Lisandro, mi hermano que me alentó a desafiarme cada día durante mi estadía en nuestra Facultad; a Yazmin, mi amiga de la infancia, el tiempo y la distancia nos han demostrado que no son retos para nuestra amistad; y, Ariadna, que me iluminó con sus risas y me ofreció su hombro en más de una ocasión. Y en general, a todos mis amigos que forman parte de mi vida.

A la Facultad de Ingeniería de la UNAM:

Por formar en mí no solo las habilidades técnicas, sino un compromiso con mi país. Honrare siempre el nombre de esta casa de estudios en mi trayectoria profesional.

CONTENTS

LIST OF TABLES

LIST OF FIGURES

LIST OF SYMBOLS

k: Absolute permeability.

q_{dh}: Volumetric flow rate.

v: Flow velocity through the porous medium.

A: Cross-sectional area.

C_{bc}: Bulk compressibility as a function of confining pressure.

C_{bp}: Bulk compressibility as a function of pore pressure.

C_r: Grain compressibility.

C_{pp}: Pore compressibility as a function of pore pressure.

C_{pc}: Pore compressibility as a function of confining pressure.

C_t: Total compressibility.

G: Shear modulus.

K_b: Bulk modulus.

$\bar{P}$: Average pressure.

P_h: Hydrostatic pressure.

P_c: Confining pressure $[psi]$.

P_p: Pore pressure $[psi]$.

V: Grain volume.

V_b^i: Bulk volume in a stress-free state.

V_p^i: Pore volume in a stress-free state.

α: Biot's coefficient.

ε_v: Volumetric strain.

E: Young's modulus.

λ: Lame's constant.

μ: Fluid viscosity.

ν: Poisson's coefficient.

ρ_r: Rock density.

$\bar{\bar{\sigma}}$: Stress tensor.

σ_{eff}: Effective stress.

σ_H: Maximum horizontal stress.

σ_h: Minimum horizontal stress.

σ_i: Principal stress.

σ_v: Vertical stress.

τ_{ij}: Shear stress.

ϕ: Porosity.

ϕ^i: Porosity in an initial or stress-free state.

∂P_c: Confining differential pressure.

dp: Differential pressure.

∂t: Differential time.

∂P_p: Pore differential pressure.

$\frac{dp}{dL}$: Pressure gradient.

∂V_p: Reduction of pore volume.

∂V_b: Reduction of bulk volume.

CHAPTER 1

1. INTRODUCTION

Each phase of a reservoir's life cycle can determine its success or inevitable failure, from the exploration of potential fields to the final-stage processes, such as enhanced oil recovery techniques. While each phase has distinct objectives, they all share a common long-term goal: achieving maximum efficiency. This represents high and optimal production (which focuses on responsible management), sustainable development with environmental care, and, crucially, substantial economic benefits for both the company and the country.

Regarding the latter, positive profit margins from oil production are essential to the economic structure of any nation based on hydrocarbon production. This impact extends to multiple areas, including trade relations with other countries, geopolitical dynamics, and social aspects, such as the quality of life for citizens. This is why oil fields must be exploited as efficiently as possible; otherwise, there is a risk of achieving the opposite.

Undoubtedly, the above offers high rewards. However, these can only be achieved through proper reservoir characterization, which seeks to determine the spatial variation of its intrinsic attributes as comprehensively as possible. These attributes include petrophysical properties, reserve dimensions, and potential risk assessments, among others. Consequently, characterization often dictates the trajectory of the entire life cycle of a reservoir.

However, this is not a simple task, as reservoirs are inherently complex systems, the challenges encountered depend on the scale and depth of the reservoir characterization required.

That said, rock compressibility is one of the most critical petrophysical properties for reservoir characterization. This is due to its key role in reservoir engineering, the design of field development, and its active involvement in enhanced recovery stages.

Compressibility plays a crucial role in the reservoir's production cycle. During the exploitation phase, the system, initially in mechanical and hydrodynamic equilibrium, becomes disturbed. This imbalance facilitates hydrocarbon extraction; however, it also leads to a significant decrease in internal pore pressure due to fluid production. As internal pressure declines, external overburden pressure and effective stress increases, resulting in pore volume reduction through compaction.

Reservoir engineers must manage this pressure differential effectively to optimize production, extend the reservoir's productive life, and mitigate potential adverse effects on the formation.

Delving deeper, compressibility is one of the five natural drive mechanisms that provide energy to the reservoir. It is known as rock-fluid expansion drive and in undersaturated volumetric reservoirs, it serves as the primary drive mechanism, contributing to the total energy delivered, according to Settari (2002). Furthermore, it is noted that neglecting compressibility effects is either impossible or at least ill-advised, given its severe impact on estimating the original oil in place (*OOIP*).

For Mexican fields, the significance of this parameter is critical. According to Rodney et. al (2019), statistical data from 16 reservoirs in the country's southwestern region revealed that 69% were volumetric and 100% were undersaturated.

Similarly, Hall (1953) emphasizes the importance of this property in volumetric material balance calculations for undersaturated reservoirs. It is critical for estimating original oil in place (*OOIP*), providing an initial approximation of recoverable reserves. This underscores the importance of rock compressibility; neglecting it compromises the entire reserve estimation process.

The determination of this property depends on the measurement scale. For large-scale studies, one commonly used technique is well logging, which generally enables the evaluation of reservoir property variations across different depths. Compressibility coefficients have been estimated using this approach by combining variations in compressible layer thickness with changes in piezometric head, employing detailed ground surface studies and multi-layer monitoring at selected

well sites, as demonstrated by Liu et al. (2004) in their research applying this technique to a field in western Taiwan.

Well-testing is another widely used technique for large-scale measurements. An example is the interference test developed by Suleen et al. (2017) for deepwater reservoirs offshore West Africa. By using analytical and numerical models, they determined both storage capacity and flow capacity. These parameters, combined with log-derived porosity, served as the foundation for calculating reservoir compressibility.

However, interference tests are not the only helpful method; buildup and drawdown tests can also analyze pressure-time curves and fit them to calculate compressibility values.

At a more advanced level, the satellite-based technique known as Interferometric Synthetic Aperture Radar (InSAR) uses radar signals to measure volumetric surface deformations. It works by emitting radar pulses into the Earth and capturing the reflected echoes. This process is continuous, enabling millimeter-scale precision in detecting changes—a capability that makes it a powerful tool now being adopted by the petroleum industry.

In their study, Jha et al. (2015) reported a coupled integrated reservoir fluid flow with a geomechanical simulator. Their paper notes that initial petrophysical property estimates were derived through probabilistic methods and joint inversion of geodetic data—specifically using InSAR technology. This coupling reduced uncertainties inherent in using either approach independently. Through rigorous mathematical and physical development, including geostatistical methods to track property evolution across space and time, they demonstrated significant reductions in ambiguity for initial property distributions (including permeability, porosity, and pore compressibility).

However, InSAR technology still presents certain limitations that must be considered. A primary constraint is noise generated by adjacent aquifers, which, if uncorrected through supplementary modeling or additional data sources, can introduce

significant uncertainty. Furthermore, multiple researchers recommend combining InSAR with global positioning measurements (e.g., GPS) to mitigate atmospheric interference that distorts InSAR signals.

The methodologies above represent some of the various approaches for large-scale compressibility estimation. It's important to note that other techniques exist, including numerical reservoir simulation and 4D seismic monitoring, for reservoir evaluation and performance prediction over time.

Although these techniques overcome many challenges at smaller scales, they still involve certain complexities, chief among them being their high costs. While laboratory-scale core extraction from fields also requires significant investment, it is generally more cost-effective in practice. Additionally, the results tend to be more adaptable, as experimental conditions can be controlled freely for sample measurements.

At more minor scales, or when core samples are unavailable for laboratory analysis, compressibility can be estimated analytically using correlations that generate type curves for each rock class. Researchers like Hall (1953), Newman (1973), and Jalalh (2006) have developed progressively more precise correlations (see **Fig. 1 - 1**). These typically express compressibility as a function of other properties, such as porosity or permeability.

However, according to Romero (2014), these analytical calculations are only recommended when experimental core data is unavailable, primarily because each correlation is typically valid under specific conditions (e.g., limited porosity ranges, rock types, or pressure/temperature windows). Additionally, they do not account for critical factors like stress effects, mineralogical distribution, or sample size.

A recent innovative technique developed by de Siqueira et al. (2018) employed X-ray microtomography-assisted digital simulation. This approach generated 3D images of plug samples from a deepwater field in Brazil, enabling the visualization of flow channels, pore size distribution, and grain morphology.

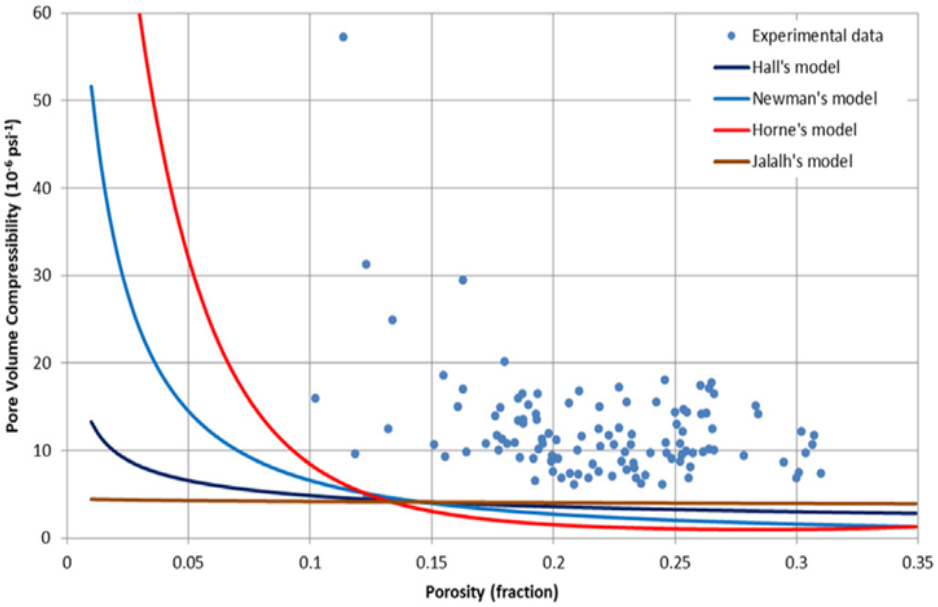

Fig. 1 - 1: Accuracy of correlations developed by various authors to calculate pore volume compressibility in sandstone (Ganat et al., 2024).

This technique aims to address limitations inherent in well logs, formation evaluation seismic, and even laboratory core tests. As the authors noted, many conventional methods fail to account for the fragility of unconsolidated samples, where even routine operations, such as core extraction, can compromise sample integrity.

Thus, their 3D imaging facilitated modeling of the apparent changes the physical sample would experience due to effective stress from hydrostatic pressure, yielding estimates closely aligned with actual reservoir conditions. However, the authors acknowledge that this technique still has unresolved limitations and unforeseen challenges, warranting further extensive research.

Continuing the ongoing discussion, when reservoir core samples are available at more minor scales, experimental tests are typically conducted to measure compressibility and other properties. The standard practice involves estimating pore volume compressibility by applying two of the four established compressibility definitions (which are discussed in **Chapter 2**).

In brief, one method evaluates compressibility as a function of pore pressure while simulating actual reservoir depletion. As pore pressure declines due to fluid extraction, with the overburden pressure held constantly, the increasing effective stress progressively compacts the pore space.

However, this specific definition presents notable challenges. First, determining the sample's saturation degree is critical, as it directly impacts the pore volume. Thus, the liquid volume recovered post-test equates to the pore volume lost during testing.

The other definition is more straightforward: it equates pore volume change to total rock volume reduction during compaction. This approach estimates pore compressibility as a function of confining pressure. Both definitions typically subject the rock to hydrostatic stress conditions.

Despite extensive research over the years and numerous efforts to understand rock-fluid interactions and the physical laws governing fluid behavior in porous media, compressibility remains a persistent challenge for the industry, with many unresolved questions, as noted by de Oliveira et al. (2016).

This stems from the fact that most studies fail to accurately replicate reservoir conditions, specifically high pressures, and temperatures. Furthermore, these experiments are typically conducted in non-representative samples, known as plug samples, with standard dimensions of 1 to 2 in in diameter and 2 to 5 in in length. Such limited sample sizes affect the estimation of the petrophysical properties.

Furthermore, few studies or technical reports address these challenges, and those that do are predominantly conducted by private companies. This situation forces PEMEX to depend entirely on external services without access to proprietary research or technological advancements. From a scientific and technological standpoint, this disparity places Mexico at a competitive disadvantage against global oil leaders.

Geomechanics is vital for understanding rock behavior under stress but is relatively new in petroleum, with only about 40 years of use. Its potential to improve reservoir

lifecycle processes is underdeveloped, causing stagnation and biased results, as seen in ongoing failures to model reservoir behavior accurately.

Therefore, this study aims to overcome current experimental limitations in compressibility analysis by proposing a novel methodology designed to solve these challenges. The methodology researches full-diameter rock samples and conducts tests under actual reservoir conditions to achieve more representative results.

The rocks come from southeastern Mexico's Pilar-Reforma-Akal Basin (**Fig. 1 - 2**). These black-oil reservoirs have depths of about 4,585 m and 3,600 m, as reported in the 2023 “Dictámenes Técnicos al Plan de Desarrollo para la Extracción" by Mexico's CNH. The main drive mechanism was rock-fluid expansion.

The selection of sandstones for this study originates from their relative homogeneity, favorable porous properties, high permeability, and notably elevated compressibility values. As Cabrera et al. (2022) demonstrated, these rocks can withstand high stress and temperature levels, making them ideal candidates for analysis.

Fig. 1 - 2: Native samples from two siliciclastic reservoirs located in the southern Gulf of Mexico.

1.1 JUSTIFICATION

This study aims to develop an experimental methodology for understanding the constitutive behavior of rock samples through compressibility tests under reservoir-like conditions.

These tests aim to enhance the experimental analysis of full-diameter core samples under high reservoir pressures and temperatures. Such tests are non-conventional, with limited published data, as even specialized multinational oilfield service companies rarely conduct them due to their technical complexity and time-intensive execution.

1.2 HYPOTHESIS

It is possible to estimate the constitutive behavior and certain elastic moduli of full-diameter samples through petrophysical tests conducted under reservoir conditions.

1.3 KEY RESEARCH OBJECTIVE

To develop a methodology for compressibility experimental measuring compressibility under reservoir conditions (e.g., average pressure of 10,000 psi and temperature above 150 °C) using full-diameter samples from a sandstone formation. Supported by petrophysical properties like permeability and porosity, the methodology estimates the elastic modulus of tested rocks.

1.4 METHODOLOGY AND RESEARCH OBJECTIVES

I. Determination of pore volume of each core sample.
II. Estimation of total and effective porosity.
III. Determination of absolute gas permeability.
IV. Experimental design and methodology for compressibility calculations.
V. Evaluation of pore compressibility as a function of confining pressure under reservoir conditions.
VI. Correlations between measured petrophysical properties.
VII. Analysis of the mechanical behavior as a function of petrophysical properties.
VIII. Calculation of the elastic modulus.

CHAPTER 2

2. LITERATURE REVIEW

This chapter explains the necessary concepts to understand compressibility and presents the literature review and methodologies for its determination.

2.1 STRESS

It is defined as the force exerted per unit area applied to a body. Unlike pressure, stress varies across different surfaces; therefore, it is possible to estimate a stress field with varying values for the same body.

In elasticity theory, principal stresses and shear (or tangential) stresses are typically distinguished because the latter are responsible for causing angular deformations. On the other hand, principal stresses—or normal stresses—are associated with the maximum and minimum stresses present in the rock.

In three-dimensional form, stress is expressed as a tensor represented by a nine-component matrix, with the main diagonal consisting of normal stresses and the non-diagonal components corresponding to shear stresses.

$$\bar{\bar{\sigma}} = \begin{bmatrix} \sigma_x & \tau_{xy} & \tau_{xz} \\ \tau_{yx} & \sigma_y & \tau_{yz} \\ \tau_{zx} & \tau_{zy} & \sigma_z \end{bmatrix}, \quad (1)$$

where:

$\bar{\bar{\sigma}}$: Stress tensor $[psi]$.

σ_i: Principal stress $[psi]$.

τ_{ij}: Shear stress $[psi]$.

According to Jaeger et al. (2007) and based on Cauchy's first postulate in solid mechanics, the matrix can be simplified by considering its symmetry, which makes it diagonalizable. As a result, only the main diagonal of the matrix is retained. Given

this, **Eq. 1** can be rewritten to explicitly represent the principal stresses in a geological medium, as follows:

$$\bar{\bar{\sigma}} = \begin{bmatrix} \sigma_v & 0 & 0 \\ 0 & \sigma_H & 0 \\ 0 & 0 & \sigma_h \end{bmatrix}, \tag{2}$$

where:

σ_v: Vertical stress $[psi]$.

σ_H: Maximum horizontal stress $[psi]$.

σ_h: Minimum horizontal stress $[psi]$.

It can be observed that σ_v is the stress that represents the lithostatic or overburden load associated with the weight of the sediment layers overlying the reservoir. This is typically the greatest of the three principal stresses in a normal faulting stress regime. On the other hand, σ_H is referred to as the maximum in-situ horizontal stress. Its magnitude depends on factors such as tectonic forces, sediment compaction, and the regional stress regime, among others. Finally, σ_h is known as the minimum horizontal in-situ stress and is often the smallest of the three. This stress is critical for understanding phenomena such as fracture propagation during matrix stimulation, wellbore stability, and production performance.

2.1.1 EFFECTIVE STRESS

First introduced by Terzaghi (1936), the effective stress concept simplifies the complex process of compaction by explaining that changes in porous volume—rather than being influenced by two variables $\{P_c$ and $P_p\}$—can be reduced to a function of a single variable: $\left(Pc - \alpha P_p\right)$. Here, P_p is the pore pressure [Pa], P_c is the confining pressure [Pa], and α is Biot's coefficient $[dimensionless]$.

According to Zimmerman (1991), this assertion is supported by considering confining pressure and pore pressure as opposing forces whose effects are reflected not only in volume reduction but also in the rock's overall petrophysical properties—such as permeability, porosity, or wave propagation velocity.

Effective stress is a critical parameter in a reservoir, as it describes the rock's mechanical behavior. This concept better understands phenomena like pore volume reduction (due to compressibility), fracturing, and faulting. Additionally, it affects key petrophysical parameters like permeability and porosity. All these properties decrease in value as fluid levels decline—that is when hydrocarbon production begins—leading to an increase in effective stress.

In summary, effective stress is the stress actually supported by the rock's solid skeleton after the contribution of the pore pressure fluid(s).

The expression that represents it is:

$$\sigma_{eff} = \sigma - \alpha P_p, \tag{3}$$

where:

σ_{eff}: Effective stress $[psi]$.

σ: Total stress applied to the rock $[psi]$.

α: Biot's coefficient $[dimensionless]$.

P_p: Pore pressure $[psi]$.

Biot's coefficient (α) quantifies the fraction of applied pressure transmitted to the pore fluid in a porous material. Its value ranges from 0 to 1; a value of 0 indicates that no pressure is transmitted to the fluid, while a value of 1 means that all applied pressure is transmitted to the fluid.

In the experimental framework, Biot's coefficient is calculated using the rock matrix's compressibility and the total compressibility under confining pressure, as follows:

$$\alpha = 1 - \frac{C_r}{C_{bc}}, \tag{4}$$

where:

C_r: Grain compressibility $[psi^{-1}]$.

C_{bc}: Bulk compressibility as a function of confining pressure $[psi^{-1}]$.

Under laboratory conditions, **Eq. 3** is adapted by considering the compressibility of the rock matrix as negligible. This is a reasonable assumption, as c_r experiences minimal deformation and thus approaches an infinitesimal size. This results in the following simplified expression:

$$\sigma_{eff} = P_c - P_p, \tag{5}$$

in which:

σ_{eff}: Effective stress $[psi]$.

P_c: Confining pressure $[psi]$.

Analyzing this issue suggests that different effective stress coefficients are necessary for various mechanical deformation processes, like pore volume compaction. This conclusion supports previous research indicating that petrophysical properties commonly change under different effective stress regimes. Therefore, relying on a single measurement of this parameter to define reservoir petrophysics is neither practical nor wise.

As mentioned earlier, several authors have researched the impact of effective stress on various rock properties. For example, Shafer et al. (2008) showed how permeability, compressibility, and elastic wave velocities (both S- and P-wave) change when assessed under varying effective stress ranges. Their study highlights the importance of effective stress in modeling pore pressure depletion-related compaction and its effects on reservoir characteristics.

Zhang et al. (2016) validated this evident dependence by creating porosity-permeability relationships as functions of effective stress for sandstones and carbonates. Their research underscores the importance of performing several measurements under differing effective stress conditions to define reservoir behavior accurately.

Petrakov et al. (2022) established correlations to determine permeability for effective stress, developing distinct models for each core sample according to grain sorting

classification. Their research examined six sandstone plugs (diameter: ~2.59 in) obtained from a Western Siberia, Russia field.

The experiment started by initial permeability determination at a reference pressure of 10 MPa, utilizing a gas permeability analyzer known as PIK-PP. The pressure was then gradually raised to a maximum of 40 MPa, which is the critical pressure threshold for the samples. Finally, the pressure decreased back to the reference level of 10 MPa, and the complete process was repeated to evaluate reproducibility and hysteresis effects.

It was concluded that permeability is a function of σ_{eff} and that the samples exhibited hysteresis behavior, indicating irreversible deformation of their structure. This deformation also impacted on other petrophysical properties, underscoring the need for further research.

2.1.2 HYDROSTATIC STRESS

This stress state occurs when a fluid surrounds a rock (or any solid material) under a pressure of magnitude P, leading to uniform stresses in all directions. This can be expressed mathematically as:

$$\sigma_v = \sigma_H = \sigma_h = P_h. \quad (6)$$

Hydrostatic stress applies a consistent load across the rock's surface, resulting in volumetric changes that are proportional in all directions **(Fig. 2 - 1)**. Experimentally, this stress condition is the benchmark for laboratory tests investigating compressibility due to its straightforward implementation.

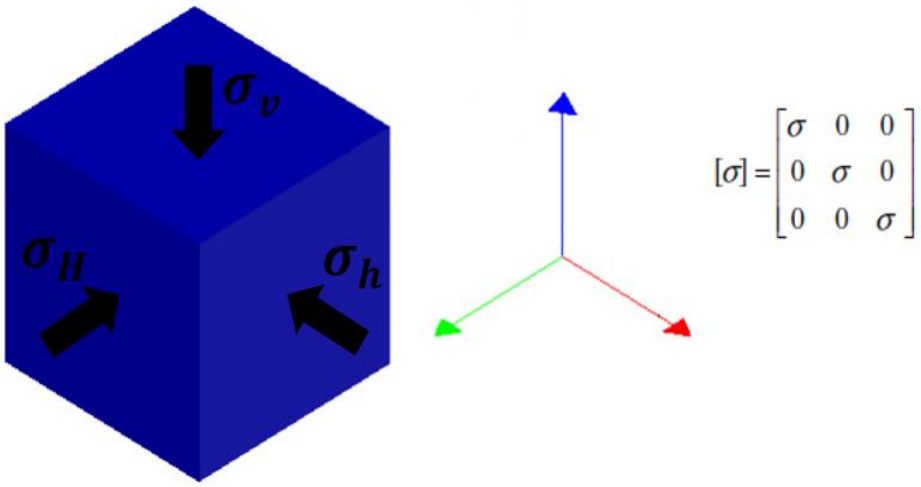

Fig. 2 - 1: An illustrated image of hydrostatic stress shows that the principal stress's value is consistent throughout the body's surfaces.

Within elasticity theory, the four definitions of compressibility (discussed later in this work) can be connected through a single boundary condition. This condition specifies a uniform hydrostatic pressure of magnitude dP_c applied to the rock's external surface, and a uniform hydrostatic pore pressure of magnitude dP_p developing within the pores, as mentioned by Zimmerman (1991). A detailed derivation is provided in **Appendix A** at the end of this document.

2.2 ABSOLUTE PERMEABILITY

Conventionally defined as the ability of a porous medium to allow the flow of a single fluid or phase through it, absolute permeability (k) is one of a reservoir's most important properties. It fundamentally determines the economic viability and production efficiency of a hydrocarbon reservoir.

According to Nelson et al. (2010), permeability is an intrinsic property of the porous medium that governs the ability of hydrocarbons and non-hydrocarbons to flow through the reservoir. It should not be confused with mobility or hydraulic conductivity. Permeability is defined in units of squared length (area), reflecting

the cross-sectional area of open pore space perpendicular to the direction of fluid flow.

French engineer Darcy (1856) proposed an empirical law to calculate permeability, stating that the fluid velocity through a porous medium is proportional to the pressure gradient. The proportionality constant in this relationship depends on the medium's absolute permeability and the fluid's viscosity.

Mathematically, velocity (v) is defined as the ratio of the volumetric flow rate (q_{dh}) to the cross-sectional area (A) through which it flows:

$$v = q_{dh}/A = -k/\mu\,(dp/dL), \tag{7}$$

where:

v: Flow velocity through the porous medium $[cm/seg]$.

q_{dh}: Volumetric flow rate $[cm^3/seg]$.

A: Cross-sectional area $[cm^2]$.

k: Absolute permeability $[D]$.

μ: Fluid's viscosity $[cP]$.

dp/dL: Pressure gradient $[atm/cm]$.

The negative sign is necessary because pressure increases in one direction while velocity increases in the opposite direction. Furthermore, the above expression is defined for single-phase fluid flow, a fluid with $1\ cp$ viscosity, a constant volumetric flow rate of $1\ cm^3/s$, a cross-sectional area of $1\ cm^2$, and under a pressure gradient of $1\ atm$ per $1\ cm$.

Likewise, the ratio q_{dh}/A is measured in velocity units and is commonly known as 'Darcy velocity', which differentiates it from the localized velocity present within individual pore channels. It is essential to highlight that permeability, similar to other rock properties, is influenced by various factors, including grain sorting, textural and geological factors, diagenetic processes, and stress-induced changes. Permeability

reacts significantly to stress variations, making it a variable factor in subsurface environments.

2.3 POROSITY

It is generally described as the ratio of pore volume to total rock volume or the non-solid portion of the rock. It is represented as:

$$\phi = \frac{Pore\ volume}{Total\ volume}, \tag{8}$$

with:

$\phi =$ Porosity $[dimensionless]$.

Since it is a property that estimates a relationship (in this case, volumes), it is typically reported as a dimensionless value or as a percentage. It can also be classified as absolute and effective porosity, the first being the total void space in the rock. At the same time, the other refers only to interconnected voids with hydraulic communication.

In the petroleum framework, porosity is a key factor in assessing hydrocarbon reserves. Consequently, various methods exist to estimate it, including geophysical logs, such as density tools and laboratory tests on core samples.

2.4 COMPRESSIBILITY

A reservoir experiences compressive stress due to the lithostatic load from the rock strata above the producing formation. The rock matrix and the reservoir fluid support this load.

The energy that enables hydrocarbon extraction, as mentioned by de Oliveira et al. (2016), is generated by disturbing the pressure differential that keeps the system in hydrodynamic and mechanical equilibrium. In other words, hydrocarbon production begins when the differential between the external pressure caused by the lithostatic load effect and the internal pore pressure from stored fluids is altered. This alteration

leads to greater overburden pressure on the pores, resulting in reduced volume due to additional formation compaction.

Zimmerman (1991) defines compressibility as the petrophysical variable that evaluates the relationship between the pressure applied to a body and the corresponding change in its volume. For a non-porous material, similar to a solid, with a single compressibility value, C, the equation is:

$$C = -\frac{1}{V^i}\frac{\partial V}{\partial P}, \tag{9}$$

where:

C: Rock compressibility $[psi^{-1}]$.

V: Rock volume $[cm^3]$.

P: Pressure exerted on the external surface $[psi]$.

i: Indicates the initial value for a stress-free environment state.

Eq. 9 can be rewritten in terms of density rather than volume, utilizing an intensive property of matter. This approach simplifies heterogeneous systems, removes unit ambiguities, aids in working with simulators, enhances integration with measured data, and streamlines calculations, among other benefits. The expression is:

$$C = \frac{1}{\rho_r^i}\frac{\partial \rho_r}{\partial P}, \tag{10}$$

in which:

ρ_r: Rock density $\left[\frac{g}{cm^3}\right]$.

The expression that represents volumetric strain is:

$$d\varepsilon_v = \frac{dV}{V^i}, \tag{11}$$

where:

$d\varepsilon_v$: Volumetric strain $[dimensionless]$.

When a reduction in volume takes place, it results in negative deformations. Likewise, a comparable expression regarding compressibility can be framed as:

$$d\varepsilon_v = -Cdp, \tag{12}$$

with:

dp: Differential pressure $[psi]$.

However, for a porous rock, the definition of compressibility assumes a different meaning, necessitating the introduction of additional terms to accurately model its physical behavior due to the complexity involved. This is because the rock is subjected to an overburden or confining pressure (P_c) acting on its external surface and to an internal or pore pressure (P_p) acting on the internal walls of the pores.

Given the above, it becomes essential to define two additional volumes to represent the changes caused by these pressures: the bulk volume (V_b), which is defined as the volume that would be measured if the rock pores were neglected, and the pore volume (V_p), representing the volume not occupied by rock minerals (**Fig. 2-2**).

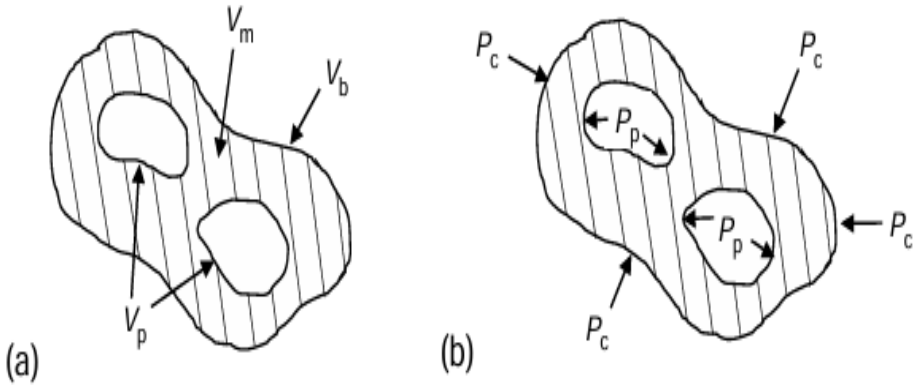

Fig. 2-2*:* Generic porous rock, showing (a) the bulk volume, pore volume, mineral/matrix volume (shaded), and (b) the pore pressure and confining pressure. (Jaeger et al., 2007).

According to research conducted by Geertsma (1957) and later revisited by Zimmerman (1991), these two pressures and volumes $\{P_c, P_p, V_b, V_p\}$ are related through linear elasticity theory. They define four distinct expressions for the compressibility of porous rock, referred to as volumetric compressibilities, as they describe the response of total volume and pore volume changes as functions of confining or pore pressure.

These expressions are distinguished by the two subscripts they involve. The first subscript refers to the type of pressure exerted, as the other pressure is kept constant. The second subscript pertains to the volume that is affected as a result of the pressure. Each of them is detailed below.

2.4.1 BULK COMPRESSIBILITY

This compressibility measures how the bulk volume changes in response to variations in confining pressure, with pore pressure held constant.

$$C_{bc} = -\frac{1}{V_b^i}\left[\frac{\partial V_b}{\partial P_c}\right]_{Pp}, \tag{13}$$

where:

C_{bc}: Bulk compressibility as a function of confining pressure $[psi^{-1}]$.

V_b^i: Bulk volume in a stress-free state $[cm^3]$.

∂V_b: Reduction of bulk volume $[cm^3]$.

∂P_c: Confining differential pressure $[psi]$.

2.4.2 BULK COMPRESSIBILITY FUNCTION OF PORE PRESSURE

This compressibility measures how bulk volume changes in response to pore pressure variations, with constant confining pressure.

$$C_{bp} = \frac{1}{V_b^i}\left[\frac{\partial V_b}{\partial P_p}\right]_{Pc}, \tag{14}$$

where:

C_{bp}: Bulk compressibility as a function of pore pressure $[psi^{-1}]$.

∂P_p: Pore differential pressure $[psi]$.

Equations **Eqs. 13** and **14** are referred to as bulk compressibilities because the volume affected in the rock is the bulk volume.

2.4.3 EFFECTIVE PORE COMPRESSIBILITY

This compressibility indicates the change in pore volume concerning variations in pore pressure while the confining pressure remains constant.

$$C_{pp} = \frac{1}{V_p^i}\left[\frac{\partial V_p}{\partial P_p}\right]_{Pc}, \tag{15}$$

where:

C_{pp}: Pore compressibility as a function of pore pressure $[psi^{-1}]$.

V_p^i: Pore volume in a stress-free state $[cm^3]$.

∂V_p: Reduction of pore volume $[cm^3]$.

∂P_p: Pore pressure differential between initial and final stages pressures $[psi]$.

Jaeger et al. (2007) states in their book that the stress-strain behavior of rocks is highly complex, even when analyzed under a single (uniaxial) stress, making it indispensable to idealize and simplify such behavior. The usual method for resolving this conflict is based on linear elasticity theory, where the deformation tensor is a linear function of the stress tensor.

The theory of linear elasticity is closely related to Hooke's Law, which states that under uniaxial tension, there is a linear relationship between axial tension and deformation, expressed as follows:

$$\sigma = E * \varepsilon, \tag{16}$$

where:

E: Young's modulus $[Pa]$.

ε: Unit strain $[dimensionless]$.

If the above expression were plotted, it would be observed that the slope of this straight line in the elastic region would be the Young's modulus.

Although rocks do not exhibit linear elastic behavior under various stresses, this approximation is valid and accurate, as many rocks behave linearly when subjected to changes in stress increments.

This explains why the compressibility of pore volume to pore pressure (c_{pp}) can be addressed using linear elasticity theory. Additionally, it plays a vital role in the mass conservation equation and, consequently, in the 1D diffusion equation, which is expressed as follows:

$$\frac{\partial P_p}{\partial t} = (k/\mu c_t)\left(\partial^2 P_p/\partial x^2\right), \tag{17}$$

with:

∂t: Time differential $[sec]$.

k: Permeability $[md]$.

μ: Viscosity $[cp]$.

C_t: Total compressibility $[psi^{-1}]$.

Total compressibility can be expressed as: $C_t = C_g S_g + C_w S_w + C_o S_o + C_{pp}$. Reservoir simulators typically calculate the fluid compressibility $C_g S_g + C_w S_w + C_o S_o$ based on phase behavior; thus, the only required variable is C_{pp}.

The definition of C_{pp}, as shown in **Eq. 15**, can be reformulated by considering reservoir boundary conditions that maintain a constant σ_v (indicating no changes in the overburden above the reservoir) and assume there are no variations in the lateral deformation ε_h, regarded as uniaxial deformation, i.e.:

$$C_{pp} = \frac{1}{V_p}\frac{dV_p}{dP_p}\bigg|_{S_v,\varepsilon_h}. \tag{18}$$

The measurement of C_{pp} is derived from effective volumetric change measurements. It is assumed that the change in pore volume dV_p is equal to the change in bulk volume dV_b, indicating that total deformation results from the change in porosity. Therefore, the equation for C_{pp} can be expressed as follows:

$$C_{pp} = \frac{1}{\frac{V_p}{V_b}}\left(\frac{1}{V_b}\frac{dV_b}{dP_p}\bigg|_{S_v,\varepsilon_h}\right). \tag{19}$$

Definition of the porosity presented by **Eq. 8**, along with the term in parentheses, signifies the total compressibility under hydrostatic conditions (noting that $\varepsilon_s = dV_b/V_b$), facilitates calculating the parameter c_{pp} in relation to the total compressibility C_{bp} using porosity.

$$C_{pp} = C_{bp}/\phi. \tag{20}$$

The total compressibility, excluding lateral deformations, roughly corresponds to the inverse of the bulk modulus ($C_{bp}{\sim}M^{-1}$). Here, M is defined as $(1-\nu)E/[(1+\nu)(1-2\nu)]$ for an isotropic elastic solid. This approximation is derived from the consideration of grain compressibility. Finally, pore compressibility can be determined using the mechanical parameters E and ν.

$$C_{pp} = \frac{(1+\nu)(1-2\nu)}{(1-\nu)E\phi}, \tag{21}$$

where:

ν: Poisson's coefficient $[dimensionless]$.

ϕ: Porosity $[dimensionless]$.

This linear elastic solid is also recognized as the most extensively utilized ideal material for stress analysis within the framework of continuum mechanics.

The linear elasticity theory is constrained as it fails to consider the visco-elastic-plastic behavior of reservoirs experiencing decline over extended periods and substantial deformations. Therefore, **Eq. 21** is utilized as a first-order approximation.

The typical values of pore compressibility range from $2 - 30 \times 10^{-6}\, psi^{-1}$. This range applies to well-cemented rocks, which demonstrate low pore compressibility $(2 \times 10^{-6}\, psi^{-1})$, whereas unconsolidated rocks tend to exhibit higher compressibility $(30 \times 10^{-6}\, psi^{-1})$.

2.4.4 PORE COMPRESSIBILITY

Termed by Hall (1953) as the formation compaction coefficient, this measure of compressibility indicates how pore volume changes to confining pressure, assuming pore pressure remains constant.

$$C_{pc} = -\frac{1}{V_p^i}\left[\frac{\partial V_p}{\partial P_c}\right]_{Pp}, \tag{22}$$

where:

C_{pc}: Pore compressibility as a function of confining pressure $[psi^{-1}]$.

∂P_c: Confining pressure differential between initial and final stages pressures $[psi]$.

2.5 BACKGROUND

Finally, this chapter presents a synthesis of the relevant work and research reviewed from international literature, some of which have been previously reported throughout the chapters.

Fatt (1958) calculated the pore compressibility in 14 sandstone cores, each 1 in in diameter and 2 in to 3 in long, which were later saturated with kerosene. The test operationally consisted of applying an external pressure that reached $10{,}000\ psi$ for several hours, after which the pressure was removed, allowing the samples to recover their original pore volume independently. This procedure was repeated a second time, reaching a maximum external pressure of 12,000 psi and internal pressure that began at 1,000 psi and increased to 10,000 psi. Finally, the external pressure was reduced to 6,000 psi, while maintaining an internal pressure of $6{,}000\ psi$, which was later decreased to 0 psi.

Mclatchie et al. (1958) conducted laboratory tests to obtain different permeability values experimentally under overburden stresses. The device used applied uniform pressure ranging from 1000 psi to 5000 psi on cores of both clean and clay-rich sandstones and limestones with slight vugs. Similarly, they were saturated with hydrocarbons driven by transmission oil.

Operationally, the test was conducted conventionally as outlined in the literature; however, the cores served as the variable factor, featuring both dirty and clean samples based on clay content. Consequently, it was concluded that for samples exhibiting low initial permeability measured at 0 psi of P_c, the reduction in permeability percentage would be significantly higher, unlike the studies carried out by Hall (1953) and Fatt (1958), among others. This suggests an opportunity to expand research on these types of cores.

Samples exhibiting hysteresis were discarded, while for the remaining samples, the relationship between pore volume and pressure was graphed, with the slope representing pore volume compressibility. The test results indicated that pore compressibility is a function of net overburden pressure (σ_v).

Dobrynin (1962) demonstrated alterations affecting properties such as compressibility, density, resistivity, elastic wave velocity, and permeability as functions of pore compressibility. Furthermore, he formulated mathematical equations that model the behavior of these petrophysical properties, all of which underwent experimental verification in two consolidated sandstones, each measuring 2 in in diameter and 5 in in length.

Operationally, pore pressure was held at atmospheric levels, while confining pressure fluctuated between 0 and 20,000 psi. A subsequent series of measurements was performed at a P_p of 1,800 psi, maintaining the same overburden pressure range.

Newman (1973) conducted a study to assess pore volume compressibility, emphasizing fragile and/or unconsolidated sandstones and limestones. In a similar vein, he examined published correlations from that era by various authors, including

Hall (1953), and Fatt (1958), among others, as he contended that there was an inadequate context, let alone correlations, focusing on unconsolidated samples.

Of the 256 rocks analyzed, 197 were identified as sandstones, while 59 were limestones. Uniform hydrostatic stress was applied to the samples with increments of $500\,psi$ until reach the reservoir lithostatic pressure. The operating temperature varied; 81 samples were at 74 $°F$, and the others ranged from 130 $°F$ to 275 $°F$.

Consequently, it was observed that the correlations established by the authors did not reflect the behavior of unconsolidated samples. After plotting the compressibilities and comparing them with existing results, a significant discrepancy was noted between the two. Additionally, a considerable variation was evident between the values for sandstone and limestone, indicating the necessity for further investigation into this subject.

Sampath (1982) introduced a technique to assess pore volume compressibility in fine-grained, quartz-rich, low-permeability sandstones from the Upper Cretaceous. This involved modifying the traditional USBM (United States Bureau of Mines) method to estimate pore volume reduction. The tests were conducted on samples known as plugs, measuring about 2 in in length and $1\,in$ in diameter. These plugs underwent temperatures between 158 and 170 $°F$, with nitrogen gas as the flowing medium. The measurements were taken under a confining pressure of 200 psi, gradually increasing to a maximum of 5,000 psi.

Andersen (1988) elaborated a methodology designed to correlate data obtained from hydrostatic stress tests and uniaxial strain tests for the estimation of pore volume compressibility. The author noted that, although it is 'simple' to conduct tests wherein the compression stress remains uniform (hydrostatic), the stresses encountered in the exploitation of any oil reservoir more closely resemble those experienced in a uniaxial test.

By employing sandstone samples with a diameter of 3 in and a length of approximately $3½$ in, and with initial stresses varying from 250 to 500 psi while utilizing strain gauges to assess deformation, the researcher was able to compare

various experimental methods and propose analytical relationships that more precisely characterize the mechanical behavior of rocks. He concluded that the majority of consolidated sandstones exhibit nonlinear elastic behavior.

Schutjens et al. (2012) developed methods to measure pore volume compressibility and porosity accurately through laboratory tests. They argue that unclear definitions for some variables in this process exist and highlight the ambiguity surrounding the accuracy of results from traditional tests that assess compressibility to confining pressure while maintaining constant pore pressure.

Using poroelasticity theory, they conducted analytical developments based in compressibility definitions, validating their equations with experimental data. They concluded that there exists a significant discrepancy between values obtained through inaccurate methods and what they consider the correct values derived from their method.

Makhnenko et al. (2013) experimentally showed that the Unjacketed Bulk Compressibility values differ between sandstone and quartz. As it was inferred, this value matched that of the primary mineral in its makeup.

Three experiments were conducted: unjacketed plane strain compression, drained compression with a water collector, and jacketed/unjacketed hydrostatic compression. All tests were performed on saturated Berea sandstone.

While the technical specifications for each test varied moderately, the results ultimately aligned, showing that the unjacketed bulk compressibility of sandstone was less than that of quartz.

Moosavi et al. (2014) formulated analytical correlations for the calculation of porosity and permeability, utilizing one sandstone and three limestones as reference rocks, in conjunction with the characteristics of pore volume compressibility.

In their porosity correlations, they derived an equation based on the initial volume and porosity of the rocks, along with two developed constants—one for the total pore modulus and the other for high-stress level compressibility. They proposed two

models for permeability: one based on the known porosity-permeability relationship known as the Kozeny-Carman relation and another as a differential approximation.

The researchers concluded that porosity and permeability depend on pore compressibility, which relies on effective stress. The proposed models show high accuracy, having been rigorously compared with experimental data. A substantial increase in effective stress leads to a moderate reduction in permeability and porosity.

de Oliveira et al. (2016) established power law connecting pore compressibility to porosity by measuring pore compressibility through uniaxial compression tests that utilized helium as the flowing medium in a porosimeter.

By using 13 plugs (six sandstones, six limestones, and one dolomite), the study revealed that for sandstones, a power law (used in the c_{pc} definition) indicated that pore compressibility decreases with increasing confining pressure and further diminishes with higher porosity, showing an almost linear, elastic-like trend. In contrast, for carbonates, two distinct behavioral trends were observed: one where pore compressibility rises as porosity declines and another where it decreases along with porosity, both exhibiting nearly inelastic behavior.

Ganat et al. (2024) established an empirical correlation to evaluate compressibility in 161 sandstone samples (121 consolidated and 40 unconsolidated) sourced from deepwater oil fields in East Asia, where lithology predominantly comprises fine grains such as clay, calcite, and quartz.

The testing concentrated on assessing permeability, porosity, and compressibility. A helium gas pycnometer determined the permeability, whereas compressibility was measured using a triaxial cell with pressures from 1 to 20 MPa. Through regression analysis, a cubic polynomial was developed to align with the trend of compressibility to porosity, using the root mean square for accuracy.

CHAPTER 3

3. EXPERIMENTAL FRAMEWORK AND DEVELOPMENT

At this point, it is crucial to document the methodology utilized for this research. However, it is essential to mention that many existing techniques primarily focus on evaluating the C_{pc} or C_{pp} under hydrostatic stress conditions. This section adheres to API standards for the procedures conducted.

The methods employ high-pressure and high-temperature equipment to apply stress to the sample. Triaxial techniques allow the variation of any of the three principal stresses—σ_v, σ_H and σ_h—enabling an anisotropic evaluation of the sample.

Furthermore, maintaining σ_h constant while varying σ_v can simulate the actual exploitation of a field where the lithological load (σ_v) changes gradually rather than abruptly, primarily due to pore pressure fluctuations that impact effective stresses and the reservoir's compressibility. In a triaxial cell setup, σ_h is typically held constant to examine how rocks respond to vertical stress or pore pressure variations.

Conversely, some cells cannot vary stress values, but this does not mean they are inefficient. In fact, they remain highly relevant, and this specific type of cell is utilized in this study. It applies hydrostatic stress to the sample, ensuring uniform strain throughout the body. Additionally, it is easier to operate and, to some extent, more cost-effective than a triaxial cell while offering straightforward result retrieval.

Similarly, the method focused on estimating the C_{pc}, which, according to Zimmerman (1991) is the ideal compressibility to be studied under laboratory conditions. This is justified by the fact that the original stresses present in the core relax when it is extracted from the reservoir. Therefore, the correct way to measure the in-situ pore volume is to return the P_c to its initial stage, that is, to the original reservoir pressure (through a scaling process).

3.1 ROCK PREPARATION AND CONDITIONING

The subsequent sections outline the procedures for operating and handling the samples involved. This includes cutting, cleaning, and packing the cores and describing the high-pressure and high-temperature equipment. The section concludes with a detailed overview of the methodologies employed and the resulting findings. These processes constitute the initial phase of the experiments, highlighting their significance and relevance to the overall success of the testing.

3.1.1 CORE TRIMMING AND CLEANING

The cores chosen for the experiments were primarily those exhibiting a satisfactory degree of isotropy and homogeneity, common characteristics of sandstone reservoirs. Additionally, the samples must be visually operative, meaning they should be free from cuts or significant fractures.

After identifying the optimal samples, they are cut to adjust their lengths and dimensions, ensuring they do not affect the cell's capacity while preserving their integrity. **Figs. 3 – 1**, **3 – 2** and **3 – 3** illustrate the handling process for the F1 sample, which follows the same procedure for the other.

Fig. 3 - 1: Measuring the core weight F1.

Fig. 3 - 2: Measuring the core length F1.

Fig. 3 - 3: Measuring the core diameter F1.

Finally, **Table 3 - 1** summarizes the dimensions of cores after being operated on.

After the samples meet the specified dimensions, they are placed in a Dean-Stark apparatus (see **Fig. 3 - 4**). This device washes and removes impurities from the samples using a cyclic distillation principle. The process involves a mixture of alcohol and toluene and generally takes about 30 days or longer, depending on the level of contamination.

Table 3 - 1: Ultimate dimensions for samples.

Assigned name	Diameter (cm)	Length (cm)	Weight (gr)
$M3$	6.6	13	770.47
$F1$	8.9	15	1869.6

Fig. 3 - 4: The Dean-Stark apparatus is observed, where the sample washing process occurs.

Once the samples are thoroughly cleaned—specifically when no impurities are visible in the alcohol and toluene mixture—they are placed in a high-temperature oven to dry for about seven days (whose average temperature was 100 °C), as shown in **Fig. 3 - 5**. This step is crucial since the fluids employed in the earlier process start to evaporate, and these vapors can be harmful.

3.1.2 CORE SLEEVING PROCESS

When the sample is prepared for operation—meaning its dimensions meet the required specifications and it is clean and dry—it is ready to be coupled to the cell. As shown in **Fig. 3 - 6**, the sleeve must endure high temperatures, pressures, and stresses; therefore, its assembly is crucial to the tests to ensure the integrity of the sample.

Fig. 3 - 5: Sample placed in a high-temperature oven to initiate the drying process.

Fig. 3 - 6: The sleeved and assembled sample is ready for laboratory testing.

3.2 EXPERIMENTAL EQUIPMENT

Table 3 - 2 outlines the functions of the equipment and apparatus utilized in this research. Subsequent paragraphs elaborate on each item, highlighting its importance in determining essential petrophysics needed for later stages and estimating compressibility values.

Table 3 - 2: Utilized equipment summary.

Equipment	Principal function	Measuring parameters	Work condition
Confining cell	Apply reservoir conditions.	Compressibility, porosity and permeability.	Pressure ranges from 0 to 20,000 psi and temperatures can reach 150 °C.
Constant flow pump	Control injection flow.	Fluid flow, injection pressure.	Range pressure from 0 to 5000 psi.
Nitrogen tank	Supply a variable gas flow.	Permeability, gas compressibility.	Range pressure from 0 to 800 psi.
Porosimeter	Record reference pressures and volumes.	Pore volume, porosity, pressure and compressibility.	Volume can reach 450 cm^3 and a pressure range from 0 to 120 psi.

3.2.1 INDIVIDUAL DESCRIPTION EQUIPMENT

1. Confining cell

This sophisticated equipment consists of various modules, such as the temperature module, the sample containment cell, and the compression module, as shown in **Fig. 3 - 7**. As stated, it can simulate reservoir conditions, with high pressures reaching up to 20,000 psi and maximum temperatures of around 150 $°C$.

2. Constant flow pump

One of its features is the capacity to connect an accumulator mounted on the top cover of the confining cell, see **Fig. 3 - 8**, allowing for the injection of the desired fluid.

In the initial phase, nitrogen gas was employed as the fluid to measure various gas-related parameters. Subsequently, in the next phase, transmission or hydraulic oil was utilized owing to its fluid properties, encompassing its ability to transmit all applied stress.

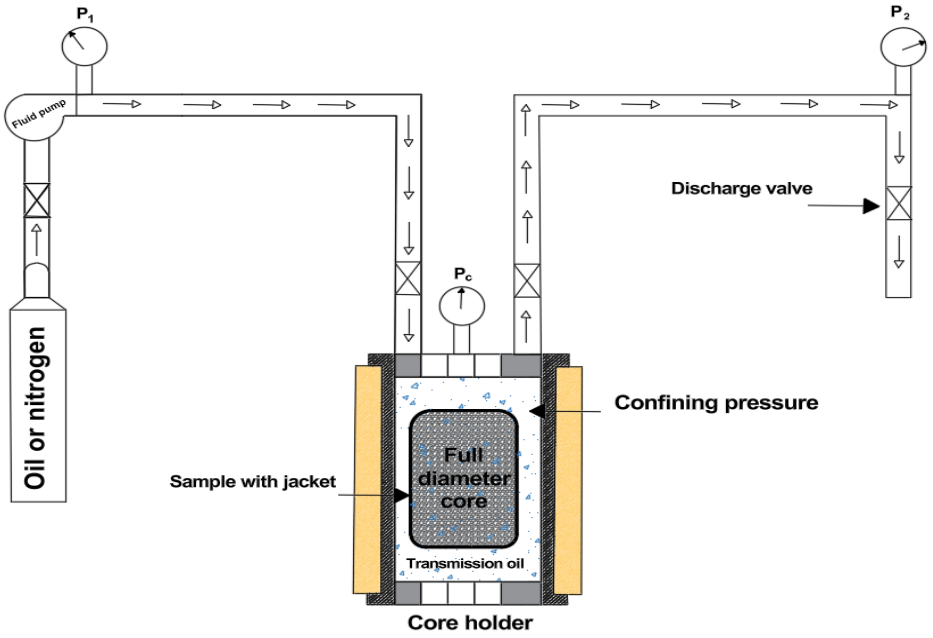

Fig. 3 - 7: Schematic representation of the cell configuration, including additional equipment.

Fig. 3 - 8: Constant flow pump utilized for oil displacement and injection into the cores.

3. Tank nitrogen

The device employed for delivering the gas stream at various stages of the experiment can inject pressures ranging from 0 to 800 psi, see **Fig. 3 - 9**. However, the porosimeter's maximum capacity is limited to 120 psi. Nitrogen gas was selected primarily because it is lightweight, colorless, and exhibits low reactivity with other elements.

4. Porosimeter

The equipment consists of two primary components: the measurement module and the tanks that serve as reference volumes, as shown in **Fig. 3 - 10**. By accurately applying Boyle's Law, the data registered by the equipment can be used to estimate pore volume, which is essential for calculating absolute and effective porosity and compressibility for gas and oil. This equipment, combined with the confining cell, can provide information to estimate these two parameters and can be evaluated under varying effective stresses, confining pressures, and temperatures.

Fig. 3 - 9: Representative photograph of the nitrogen tank used.

Fig. 3 - 10: Photograph of the porosimeter used at various experiment stages.

3.3 EXPERIMENT PROTOCOL

This section provides an explanation of the experimental methods along with the results obtained. However, because two distinct types of fluids were employed to evaluate the properties of interest, this section has been divided into two subsections.

3.3.1 GAS METHODOLOGY

PHASE 1. ASSEMBLY IN THE CONFINING CELL

The aim at this stage is to create the conditions for the experiment, ensuring no operational issues could hinder its proper execution.

Once the sample is appropriately sleeved and verified to be free of any leaks within the arrangement, it is deemed ready to proceed with experimental procedures, which commence upon its introduction into the confining cell.

Upon introducing the sample into the cell, it was noted that it became surrounded by the transmission oil, as visually depicted in **Fig. 3 - 7**. Subsequently, the cover was secured with the outlets that facilitate the injection or expulsion of fluids. The pressure, P_c, was then incrementally increased to verify the presence of leaks further. Should any leaks exist, it would be observable how the oil begins to escape from the cell cover, thereby representing a complete contamination of the sample and, consequently, compromising the integrity of the experiment.

Otherwise, the presence of oil should be non-existent. Therefore, the core is adequately positioned.

PHASE 2. PORE VOLUME MEASUREMENT

After verifying the integrity of the equipment that interacted with the sample, the P_c was successively increased. This affects directly the effective stress, allowing for the measurement of property values at each stage based on the applied stress.

To determine the V_p, a constant P_c of approximately 1000 psi was applied to circulate a gas flow continuously through the rock. This V_p measurement is crucial as it is a reference for related calculations.

Measuring V_p is essential because compressibility quantifies the reduction of this parameter. Compressibility can be expressed in terms of density, porosity, or volume. Thus, having an original or reference volume is crucial for determining volume reductions.

As a result, a well-known method for determining V_p involves applying Boyle's law via the expansion of a gas, utilizing a porosimeter and a nitrogen tank. The logic is straightforward, as the gas is contained within a chamber of known volume (V_1) and pressure (P_1). This chamber is connected to the confining cell. Upon opening the valve that previously restricted the flow, the gas expands to fill the porous volume of the sample. Consequently, a second pressure (P_2) is achieved at equilibrium. Subsequently, it is necessary to calculate the missing volume V_2, which typically corresponds to V_p at 1000 psi, as illustrated in **Fig. 3 - 11**.

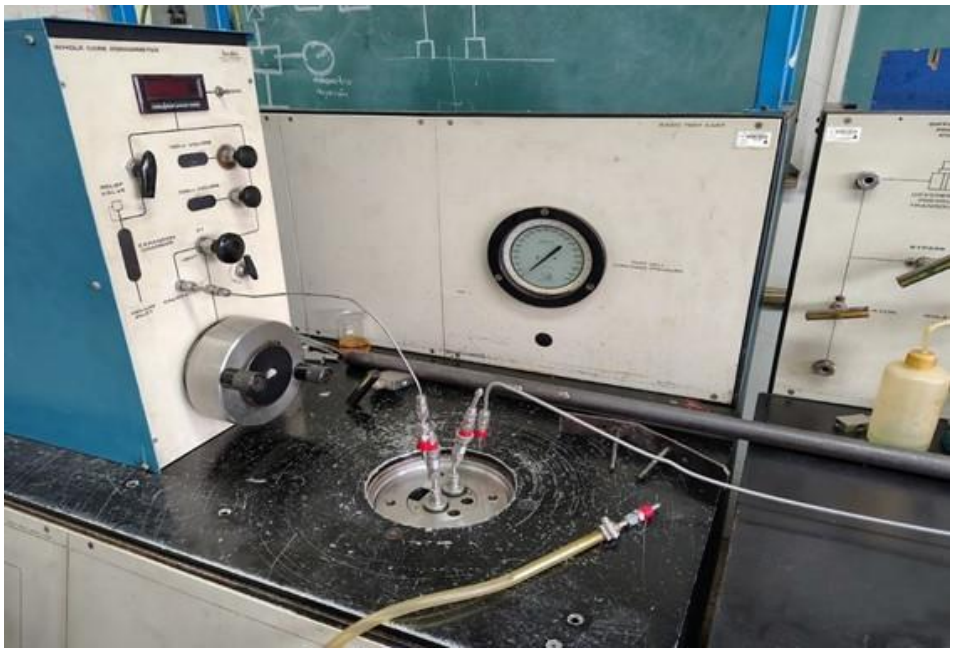

Fig. 3 - 11: Schematic photo of the arrangement used to measure V_p with gas.

As stated earlier, this process was conducted gradually in intervals, where V_p values were recorded from 1000 to 1000 psi until 12,000 psi. **Table 3 - 3** summarizes these values for sample M3, indicating that some were excluded because they did not align with the observed trend, which was attributed to the uncertainty in the experimental measurements. Following this, **Fig. 3 - 12** illustrates the decreasing V_p values as P_c increases.

Table 3 - 3: Pore volume (V_p) behavior using gas recorded at different P_c for sample M3.

Confining pressure $(\boldsymbol{P_c})$ $\boldsymbol{psi}$	**Pore volume** $(\boldsymbol{V_p})$ $\boldsymbol{cm^3}$
$\mathbf{1000}$	53.23
$\mathbf{3000}$	53.35
$\mathbf{4000}$	52.69
$\mathbf{5000}$	52.97
$\mathbf{6000}$	52.75
$\mathbf{9000}$	51.39
$\mathbf{10,000}$	51.20
$\mathbf{11,000}$	51.12
$\mathbf{12,000}$	50.85

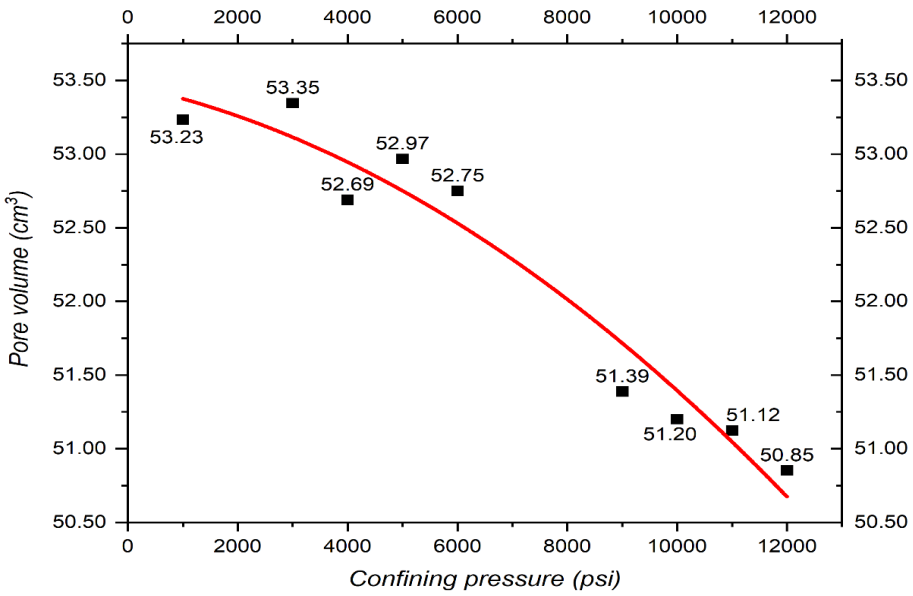

Fig. 3 - 12: Pore volume as a function of confining pressure for sample M3.

PHASE 3. POROSITY MEASUREMENT

The absolute porosity was estimated using the definition of porosity given in **Eq. 8**, which incorporates the longitudinal characteristics of the samples alongside the reference V_p value at 1000 psi. Operationally, this step resembles the previous one in measuring pore volume, as the equipment setup remained consistent, and the same physical principle was utilized. The absolute porosity results for core M3 are presented in **Table 3 - 4**.

The absolute porosities indicate the maximum values for these parameters measured under laboratory conditions regardless of the fluid used.

Conversely, the effective porosity values were determined based on various effective stresses and reservoir temperatures. The method involved stabilizing the porosimeter at a reference volume and pressure. Once calibrated, it was connected to the confining cell set to 1000 psi. Subsequently, the valve was opened to release gas from the cell. After the pressure stabilized, the porosimeter recorded the value, and this process was repeated at least three times to ensure accurate results.

Upon the completion of approximately 90 repetitions, the porosimeter was disconnected from the cell, and the effective stress was gradually increased to 2000 psi to replicate the aforementioned procedure. This process continued until the effective stress reached 12,000 psi. Outliers or values deviating from the central tendency were excluded to ensure a more precise trend. The results are presented in **Table 3 - 5**, while **Fig. 3 - 13** illustrates the trend of the effective ϕ values to P_c.

Table 3 - 4: The absolute porosity value for M3 core for an effective stress of 1000 psi.

Core	**Porosity** $(\boldsymbol{\phi})$ $\boldsymbol{dimensionless}$
M3	0.1196

Table 3 - 5: Measurement of effective gas porosity for sample M3.

Confining pressure $(\boldsymbol{P_c})$ $\boldsymbol{psi}$	**Porosity** $(\boldsymbol{\phi})$ $\boldsymbol{dimensionless}$
$\mathbf{1000}$	0.1196
$\mathbf{3000}$	0.1199
$\mathbf{5000}$	0.1190
$\mathbf{6000}$	0.1186
$\mathbf{9000}$	0.1155
$\mathbf{10,000}$	0.1151
$\mathbf{11,000}$	0.1149
$\mathbf{12,000}$	0.1143

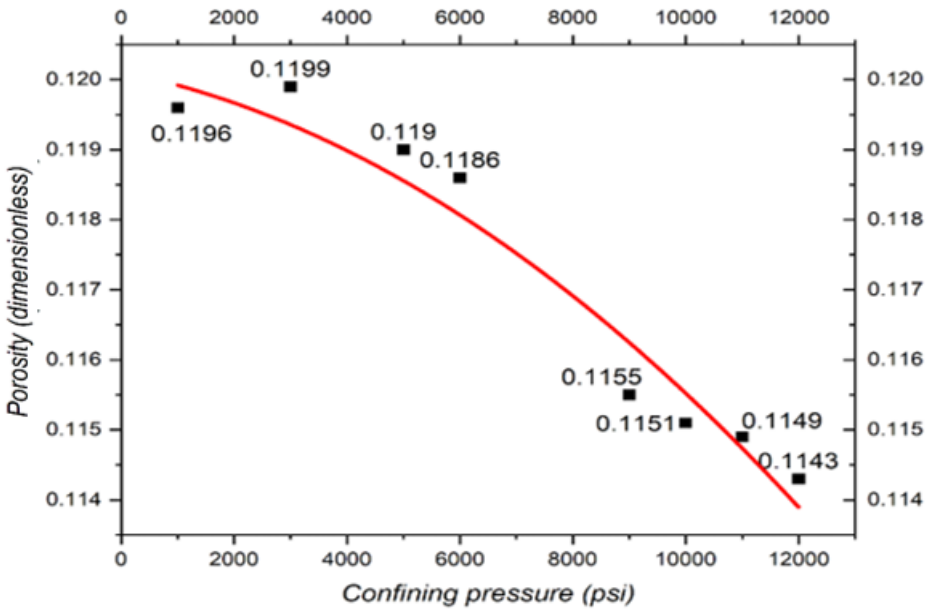

Fig. 3 - 13: Measurement of effective gas porosity as a function of confining pressure for sample M3.

PHASE 4. PERMEABILITY MEASUREMENT

The method for estimating absolute gas permeability utilized the experimental setup from previous stages. The nitrogen tank was connected to the confining cell, allowing gas to flow through the sample at a specified injection pressure under variable effective stresses. The system's outlet, open to the atmosphere, recorded these values using a flowmeter.

The values recorded by the flowmeter should be interpreted as a preliminary estimate of the sample's absolute gas permeability; however, they cannot be regarded as definitive without first correcting for several parameters that influence the gas's behavior and are not controlled by the equipment.

These factors include the Klinkenberg effect, often referred to as the gas slip effect, and flow turbulence phenomena, which are accounted in the turbulence coefficient. Thus, it is essential to apply these corrections to achieve precision in the experimental data analysis.

In detail, the operations conducted on sample M3 involved a stepwise increment of the P_c at differential pressures of Δ1000 psi. Initially, a P_c of 1000 psi was established within the cell, followed by the circulation of a gas stream at an injection pressure that commenced at 30 psi and increased to 90 psi, with permeability values recorded at intervals of Δ10 psi. This process was repeated until a confining pressure of 12,000 psi was attained, resulting in approximately 80 readings.

After obtaining the permeability values and correcting for the previously described phenomena, a graph shows their relationship as a function of effective stress. **Table 3 - 6** below summarizes this data; it's important to note that values not conforming to the indicated trend have also been omitted.

Finally, **Fig. 3 - 14** illustrates the trend recorded for sample M3 to provide a graphical representation.

Table 3 - 6: Gas permeabilities at various effective stress levels in sample M3.

Confining pressure (P_c) psi	**Permeability** (k) md
1000	234.01
3000	211.53
4000	183.23
5000	174.4
7000	143.11
10,000	93.82
11,000	92.11
12,000	63.73

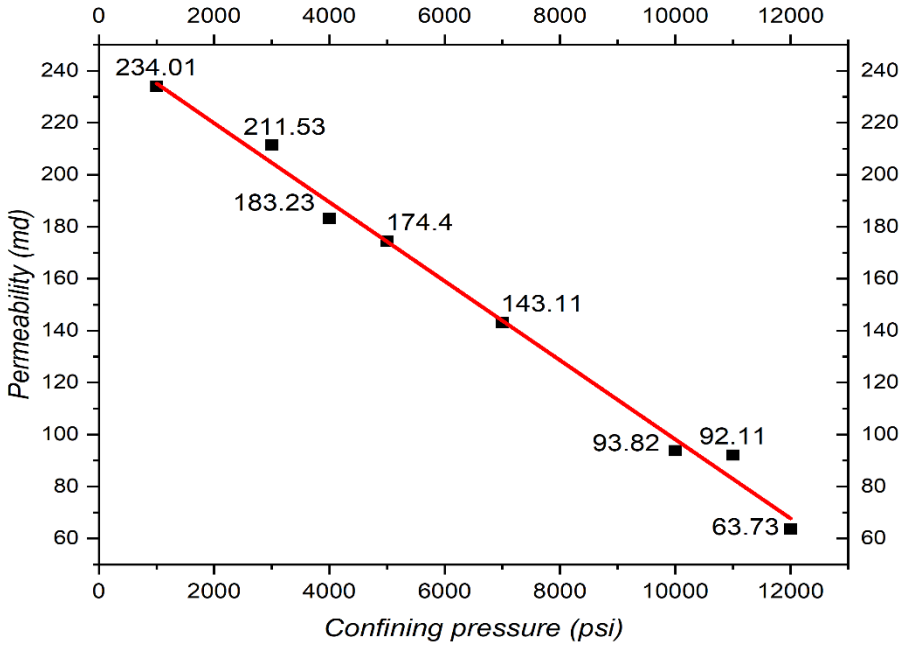

Fig. 3 - 14: Permeability values as a function of effective stress for sample M3.

PHASE 5. COMPRESSIBILITY MEASUREMENTS

A detailed examination of expression **Eq. 22**—defined as the compressibility equation by Zimmerman (1991)—allows for calculating C_{pc} as a function of effective stress and another property, like ϕ or V_p, which has already been derived. In this instance, the values of V_p were utilized. Below is **Table 3 - 7**, which presents the approximate values of compressibility as a function confining pressure.

Please note that the range for the P_c differs significantly from that utilized in prior procedures. The rationale for this discrepancy is attributed to the values for the C_{pc} associated with these P_c being considerably removed from the minimal trend that could be perceived. Consequently, it was determined that these values should be excluded. **Fig. 3 - 15** illustrates the trend generated.

Table 3 - 7: Estimated values of C_{pc} as a function of effective stress for the sample M3.

Confining pressure (P_c) psi	**Compressibility (C_{pc})** psi^{-1}
9000	$8.53x10^{-6}$
10,000	$3.51x10^{-6}$
11,000	$1.44x10^{-6}$

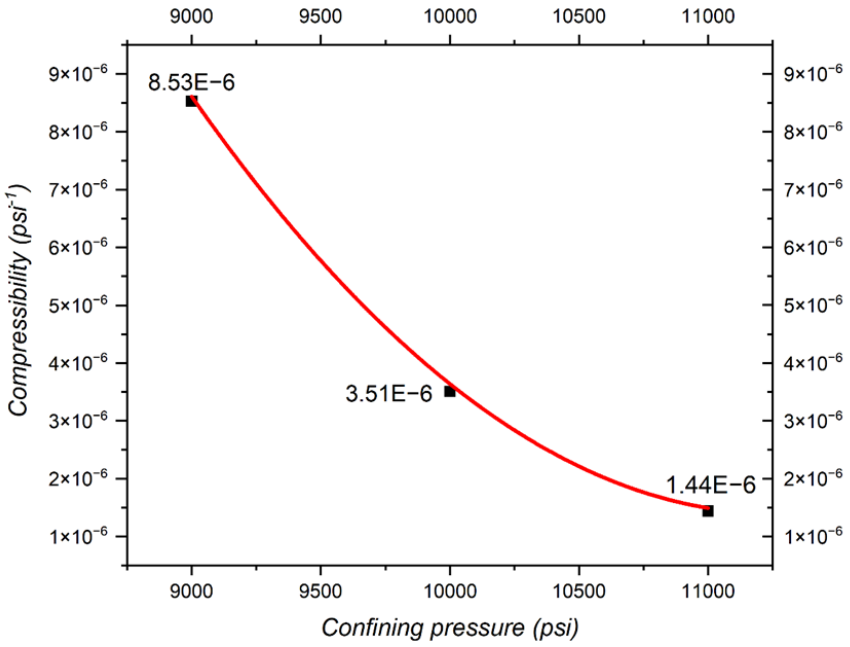

Fig. 3 - 15: Relationship of C_{pc} as a function of P_c for sample M3.

3.3.2 OIL METHODOLOGY

PHASE 1. ASSEMBLY IN THE CONFINING CELL

This method's cell configuration was identical to the earlier gas-based methodology.

PHASE 2. OIL SATURATION

In contrast to the preceding methodology, this section must begin by elucidating the oil saturation process of the samples, as this is necessary for estimating the properties of interest.

The configuration employed included an accumulator with injection capacity of 500 ml of transmission oil. This accumulator was connected to the constant flow pump, which facilitated the displacement of the oil volume to the confining cell, where the sample was already contained.

The confining cell was maintained at a constant pressure of 1000 psi, similar to previous stages. However, this time, an average temperature of 120 $°C$ was applied, and the system was opened.

The test began when a small portion of the oil was displaced under low constant injection pressure. Since the system was open, it facilitated the observation of the exact moment when the first drop of oil traveled through the injection lines, entered the core, and passed through the outlet lines (see **Fig. 3 - 16**). This moment indicated that the system needed to be closed.

Just because the oil has completely moved through the system doesn't ensure that the pore volume of the samples is filled with oil. Instead, it indicates that the sample possesses good permeability, allowing fluid to flow freely, which is why the system was closed.

Following the system closure, a small amount of oil was injected, and stabilization was ensured to prevent re-pressurization. Once sufficient time had passed (between 5 to 10 minutes), the system was opened, and a moderate amount of oil was released compared to the initial injection, indicating that the sample was saturated correctly.

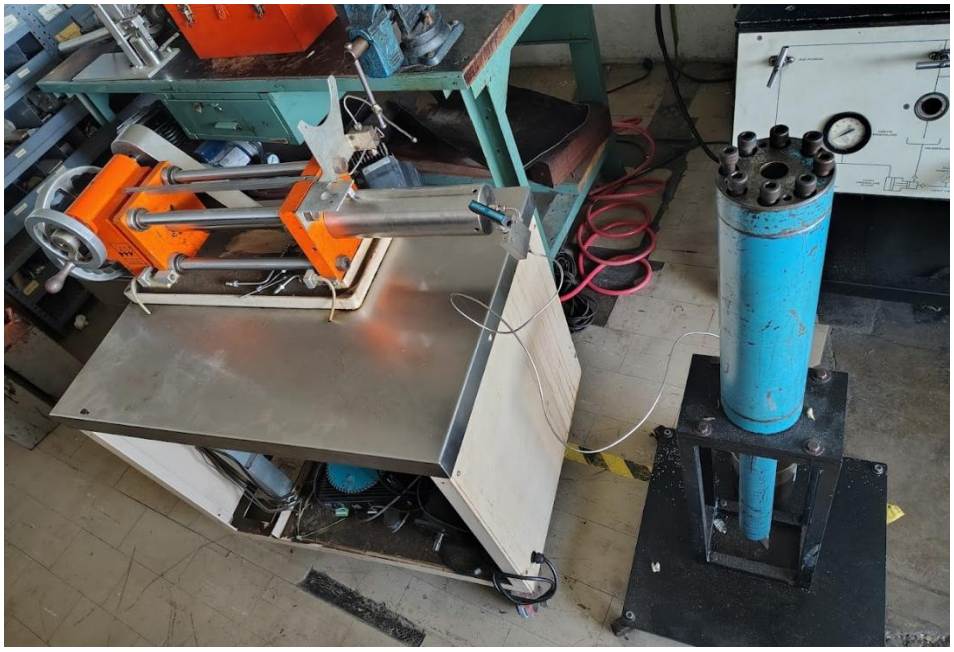

Fig. 3 - 16: The system consists of the constant-flow pump, the oil volume accumulator, and the confining cell where it is contained and connected.

This process continues until 500 ml of oil was displaced. However, it's important to note that the total volume injected may not be fully recovered at the outlet; some of it remains in the lines connected to the equipment, and a portion remains in the V_p of the samples. Ultimately, **Fig. 3 - 17** illustrates the volume recovered after this process, marking the end of this stage.

Phase 3. Pore volume measurement

After accurately measuring the line volume and the recovered volume from the previous step, a straightforward calculation was performed to find the difference between these two values, facilitating the inference of V_p for both samples.

In the oil methodology, the P_c differential for each point differed from that used in the gas methodology. For sample $M3$, the increment value was $\Delta 3000\ psi$, while for sample $F1$, it was $\Delta 2000\ psi$. Results are detailed in **Tables 3 – 8** and **3 – 9**.

Figs. 3 – 18 and **3 – 19** illustrate the relationship between V_p as a function of effective stresses.

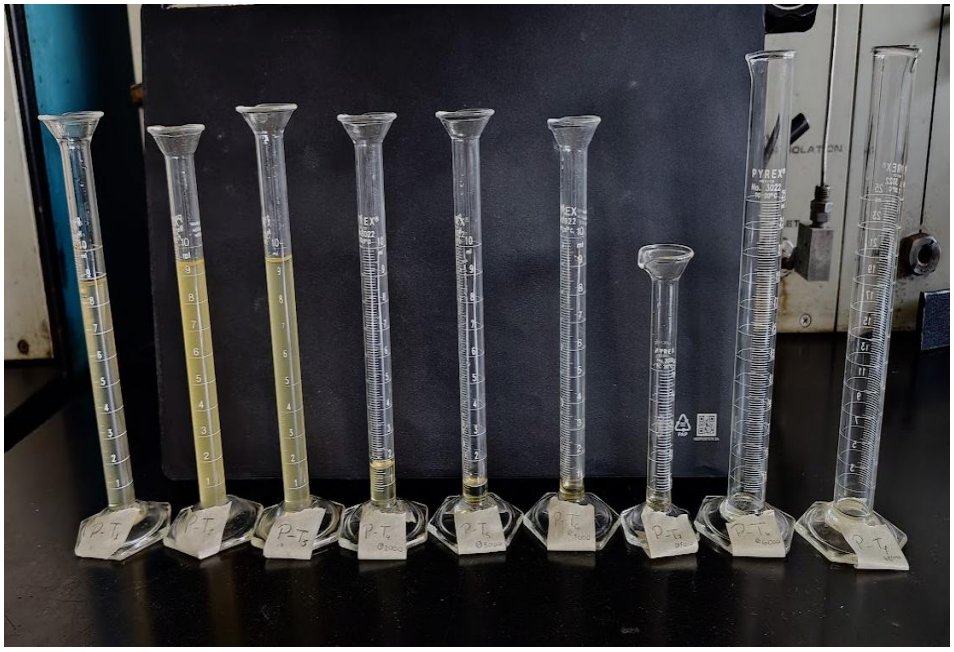

Fig. 3 - 17: Volume recovered after core saturation for the sample M3.

Table 3 - 8: Pore volume (V_p) values for core M3.

Confining pressure (P_c) psi	**Pore volume** (V_p) cm^3
1000	66.00
4000	61.20
7000	59.30
10,000	57.70
12,000	57.00

Table 3 - 9: Pore volume (V_p) values for core F1.

Confining pressure (P_c) psi	Pore volume (V_p) cm^3
1000	188.70
3000	186.60
5000	182.30
7000	177.70

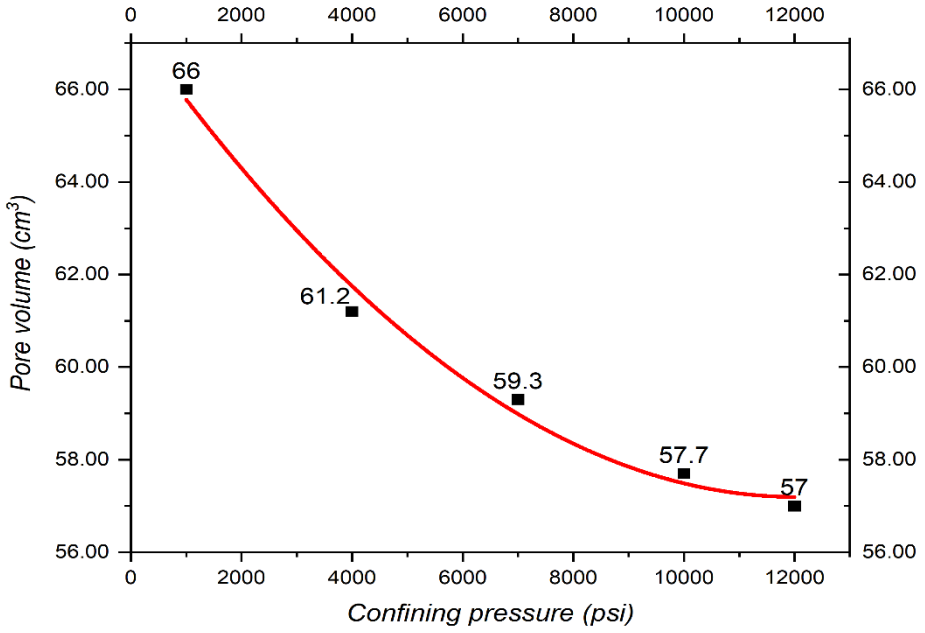

Fig. 3 - 18: Behavior of V_p as a P_c function using oil for sample M3.

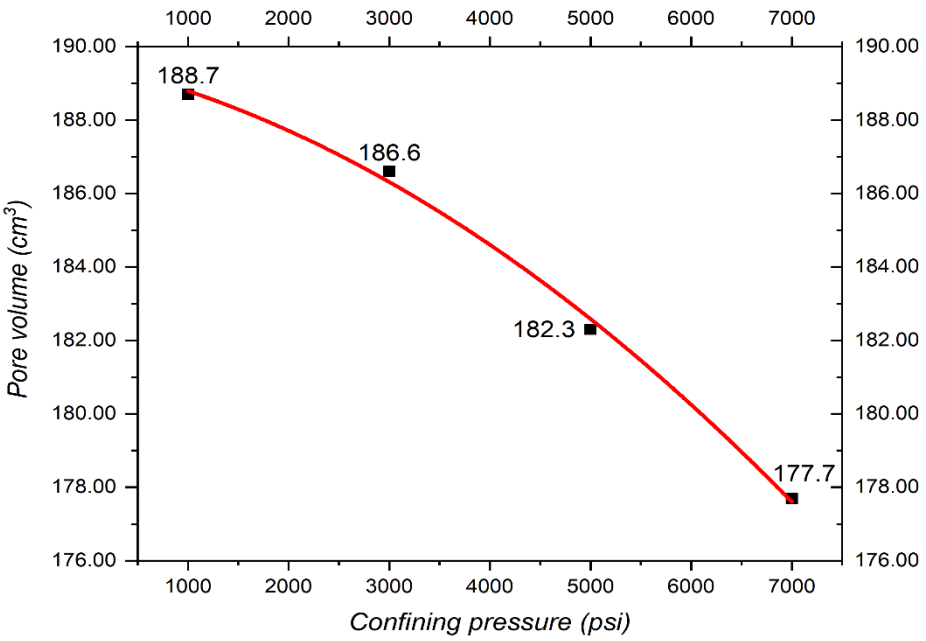

Fig. 3 - 19: Behavior of V_p as a P_c function using oil for sample F1.

Phase 4. Porosity measurement

The methodology employed to estimate the absolute porosity as a function of gas is analogous to that utilized in this section. Using the longitudinal characteristics and referencing V_p at 1000 psi, the total porosity values were determined for samples M3 and F1, with the results documented in **Table 3 - 10**.

Regarding effective porosity, the volumes of recovered oil—resulting from the increase in effective stress during the next stage of compressibility—were compared with the reference V_p. This comparison is summarized in **Tables 3 – 11** and **3 – 12**:

Table 3 - 10: Absolute porosity values for cores M3 y F1.

Core	Porosity (ϕ) $dimensionless$
M3	0.1484
F1	0.2022

Table 3 - 11: Effective porosity values for core M3.

Confining pressure $(\boldsymbol{P_c})$ $\boldsymbol{psi}$	**Porosity**$(\boldsymbol{\phi})$ $\boldsymbol{dimensionless}$
$\mathbf{1000}$	0.1484
$\mathbf{4000}$	0.1376
$\mathbf{7000}$	0.1333
$\mathbf{10,000}$	0.1297
$\mathbf{12,000}$	0.1282

Table 3 - 12: Effective porosity values for core F1.

Confining pressure $(\boldsymbol{P_c})$ $\boldsymbol{psi}$	**Porosity** $(\boldsymbol{\phi})$ $\boldsymbol{dimensionless}$
$\mathbf{1000}$	0.2022
$\mathbf{3000}$	0.1999
$\mathbf{5000}$	0.1953
$\mathbf{7000}$	0.1904

Figs. 3 – 20 and **3 – 21** illustrate the effective porosity in relation to various stated effective stresses, for both sample types.

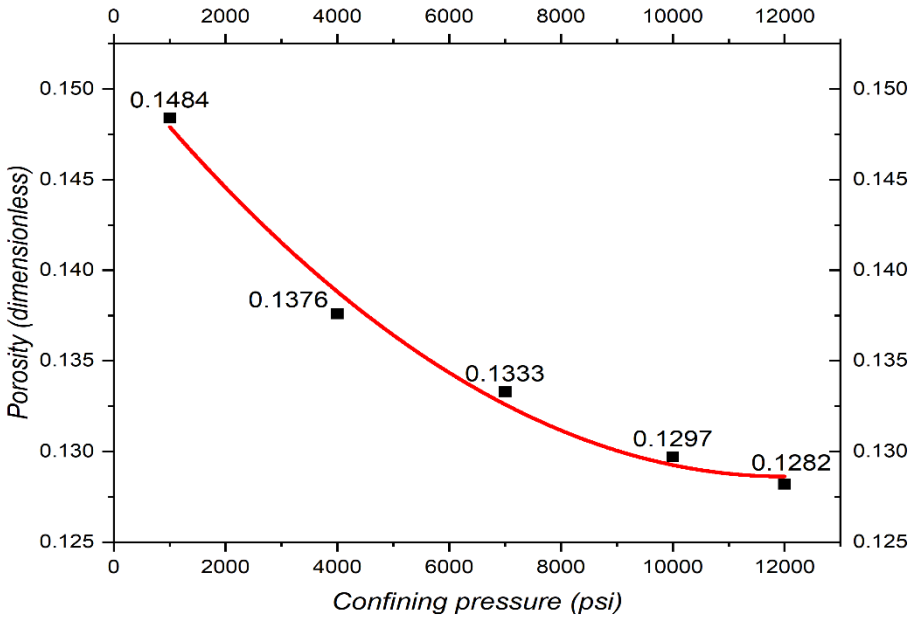

Fig. 3 - 20: Ratio of effective porosity to effective stress for sample M3.

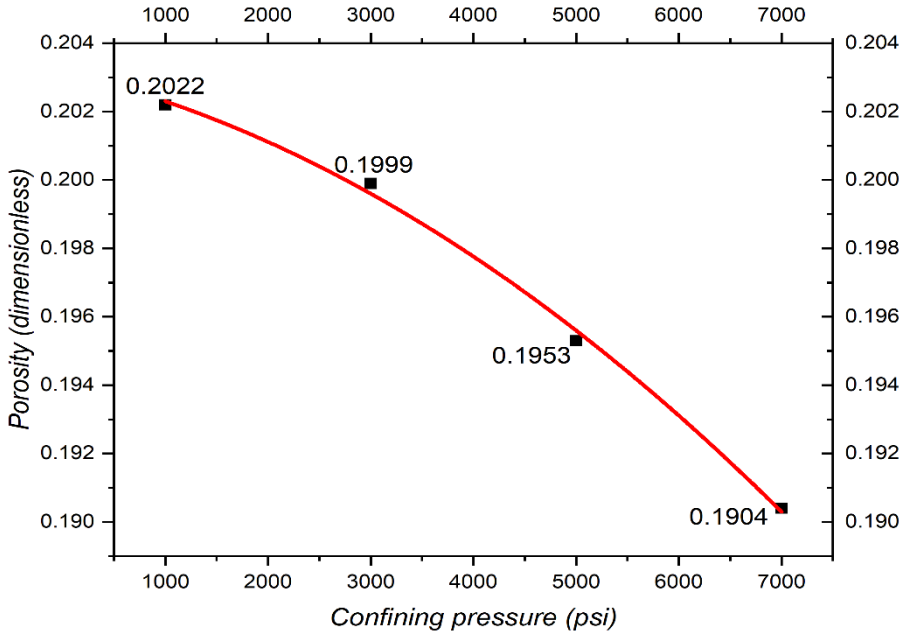

Fig. 3 - 21: Ratio of effective porosity to effective stress for sample F1.

Phase 5. Compressibility measurement

In this final stage, the setup is only modified by disconnecting the equipment and retaining only the outlet connections and pressure gauges. Given that fluid expulsion is anticipated; including graduated containers for measuring the output is recommended, as illustrated in **Fig. 3 - 22**.

The test started by closing the system and raising the P_c from 1000 psi to 4000 psi. This was done to ensure that the retrieved fluid represented the product of the final pressure increase. After this, the system was opened, and a specific volume of recovered oil was collected. This volume is crucial for understanding the compaction degree of the V_p in the rocks; so, it must be accurately measured and preserved.

The experiment proceeded by raising the P_c via scaling, applying a pressure differential of Δ3000 for sample M3 and Δ2000 for sample F1, and was concluded once 12,000 psi was achieved.

Fig. 3 - 22: Test tube added at the end of the setup to collect the volume expelled and/or recovered.

After accounting for the volume recovered at each stage, **Eq. 22** estimated the compressibility values based on confining pressure, maintaining a constant pore pressure. The findings for each sample are presented in **Tables 3 – 13** and **3 – 14.**

Table 3 - 13: Volume recovered through compaction processes and the estimated C_{pc} values for sample M3.

Confining pressure (P_c) psi	**Recovered volume** cm^3	**Compressibility** (C_{pc}) psi^{-1}
1000	0	–
4000	4.8	$24.24x10^{-6}$
7000	1.9	$9.6x10^{-6}$
10,000	1.6	$8.08x10^{-6}$
12,000	0.7	$5.3x10^{-6}$

Table 3 - 14: Volume recovered through compaction processes and the estimated C_{pc} values for sample F1.

Confining pressure (P_c) psi	**Recovered volume** cm^3	**Compressibility** (C_{pc}) psi^{-1}
1000	0	–
3000	2.1	$5.56x10^{-6}$
5000	4.3	$11.39x10^{-6}$
7000	4.6	$12.18x10^{-6}$

Figs. 3 – 23 and **3 – 24** provide a detailed visualization of how these values behave to the various effective stresses.

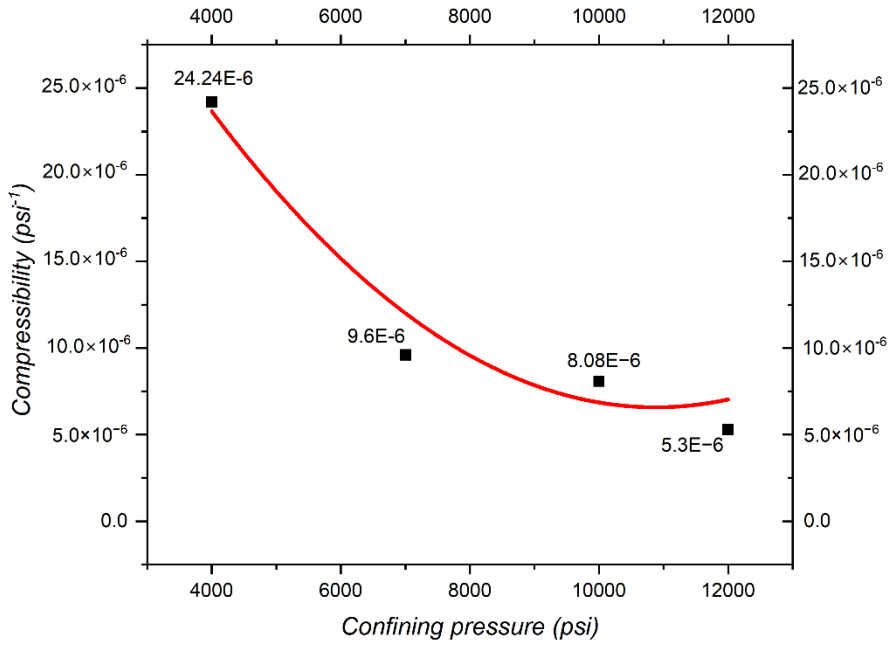

Fig. 3 - 23: C_{pc} as a function of effective stress for sample M3.

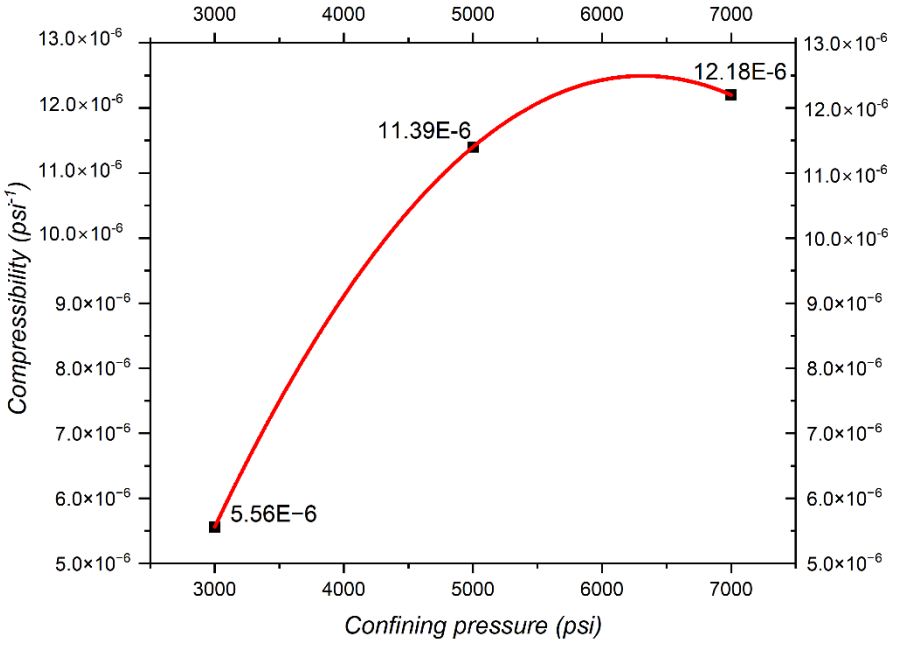

Fig. 3 - 24: C_{pc} as a function of effective stress for sample F1.

CHAPTER 4

4. DATA INTERPRETATION AND DISCUSSION

The analysis of results represents a critical phase of this work, as it elucidates the procedures employed to process, visualize, and interpret the compressibility data and its correlation with porosity and permeability. Furthermore, it provides the foundation for formulating an expression that describes strain as a function of compressibility, in order to formulate a constitutive model.

The aforementioned procedures uphold the essential integrity of the data collected from experiments and are expressed through correlations that accurately model the observed trends in the curves. In simpler terms, the formulated expressions that support the study's analytical component are grounded in data obtained from the experimental process.

It is essential to note that the established correlations mainly consist of polynomial curves (although linear and exponential models were also used), with their statistical approach based on least squares regression. These models were selected due to their apparent simplicity and practicality; their purpose is to serve as tools that facilitate the visualization of property behaviors.

It should be noted that the atypical behavior of sample F1 is discussed in the final section of this chapter, where some explanations for this behavior are suggested.

Before this, **Tables 4 – 1** and **4 – 2** present a summary of the values obtained for the properties of samples M3 and F1, respectively:

Table 4 - 1: Summary of the properties obtained throughout the experiment for sample M3; permeability was the only one reported using nitrogen gas.

Properties				
Confining pressure (P_c) psi	**Pore volume** (V_p) cm^3	**Porosity** (ϕ) $dimensionless$	**Permeability** (k) md	**Compressibility** (C_{pc}) psi^{-1}
1000	66.00	0.1484	234.01	–
3000	–	–	211.53	–
4000	61.20	0.1376	183.23	$24.24x10^{-6}$
5000	–	–	174.4	–
7000	59.30	0.1333	143.11	$9.6x10^{-6}$
10,000	57.70	0.1297	93.82	$8.08x10^{-6}$
11,000	–	–	92.11	–
12,000	57.00	0.1282	63.73	$5.3x10^{-6}$

Table 4 - 2: Summary of the properties obtained throughout the experiment for sample F1; the permeability values were excluded due to an unusual trend.

Properties			
Confining pressure (P_c) psi	**Pore volume** (V_p) cm^3	**Porosity** (ϕ) $dimensionless$	**Compressibility** (C_{pc}) psi^{-1}
1000	188.70	0.2022	–
3000	186.60	0.1999	$5.56x10^{-6}$
5000	182.30	0.1953	$11.39x10^{-6}$
7000	177.70	0.1904	$12.18x10^{-6}$

Although the permeability values for sample F1 were corrected using the same procedure described in the permeability measurement section, the trend remained erratic, possibly associated with the atypical behavior founded in the sample; this is the reason why those values were omitted.

4.1 INTERPRETATION OF COMPRESSIBILITY DATA

As **Appendix A** outlines, the four definitions of compressibility can be connected by assuming that the rock matrix behaves like an isotropic, homogeneously elastic material. This assumes that uniform hydrostatic pressure acts both within the pores and on the external surface, as Jaeger et al. (2007) noted.

The preceding leads to the following expression:

$$C_{pp} = C_{pc} - C_r. \tag{23}$$

For practical purposes, C_r is very small and thus negligible in this experiment, which simplifies **Eq. 23** as:

$$C_{pp} \approx C_{pc}. \tag{24}$$

Conversely, utilizing:

$$C_{pc} = (C_{bc} - C_r)/\phi^i, \tag{25}$$

where:

ϕ^i: Porosity in an initial or stress-free state $[dimensionless]$.

By neglecting once more the effects of C_r and removing C_{bc} from the expression in **Eq. 25**, it obtains:

$$C_{bc} = C_{pc}\phi^i. \tag{26}$$

Now, using:

$$C_{bp} = C_{bc} - C_r. \tag{27}$$

Neglecting to C_r the expression beforehand results in:

$$C_{bp} \approx C_{bc}. \tag{28}$$

So:

$$C_{bp} \approx C_{bc} \approx C_{pc}\phi^i. \tag{29}$$

Consequently, the expressions derived from **Eqs. 24** and **29**, when illustrated as a function of effective stress, enable visualization of the previously mentioned relationship among several definitions of compressibility. The experimental data also corroborates this, noting that these values indicate C_{pc}, which facilitates inference of the other definitions.

Figs. 4 – 1 and **4 – 2** illustrate the compressibility behavior for samples M3 and F1 when using oil, respectively.

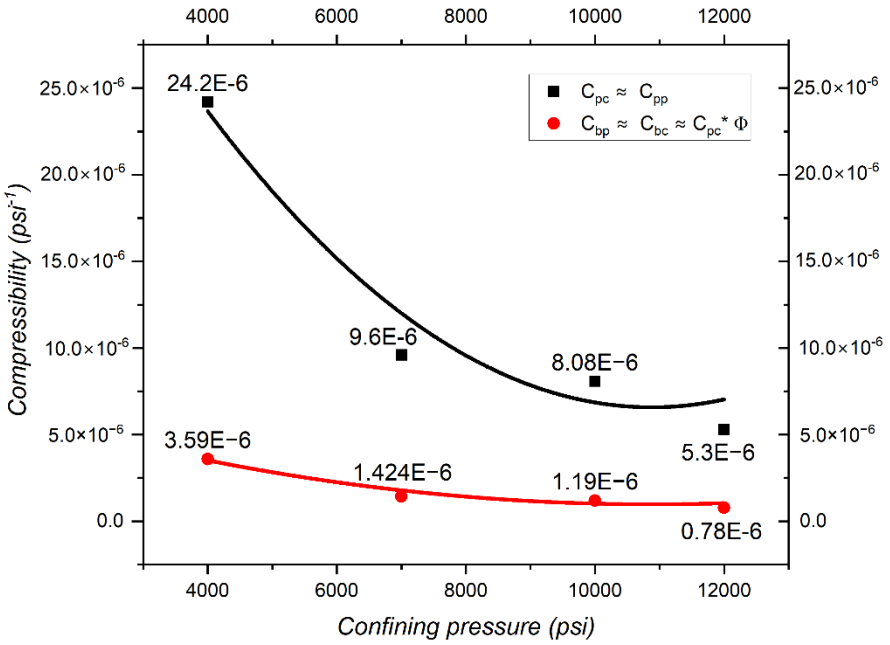

Fig. 4 - 1: Comparison of compressibilities using oil for sample M3: red curve shows the trend of bulk compressibilities, while black curve depicts the behavior of pore compressibilities.

Regarding qualitative behavior, the typical relationship between compressibility and effective stress is evident; as P_c rises, the reduction in volume slowly decreases. In the earlier stages, the highest coefficients of compressibility were observed since there is a greater V_p to experience deformations.

This is more evident in the pore compressibilities, C_{pc} and C_{pp}, as the pore volume experiences a larger impact from applied stresses, leading to greater compaction. Conversely, the bulk compressibilities, C_{bc} and C_{bp}, show lower values because the matrix does not deform significantly due to these stresses.

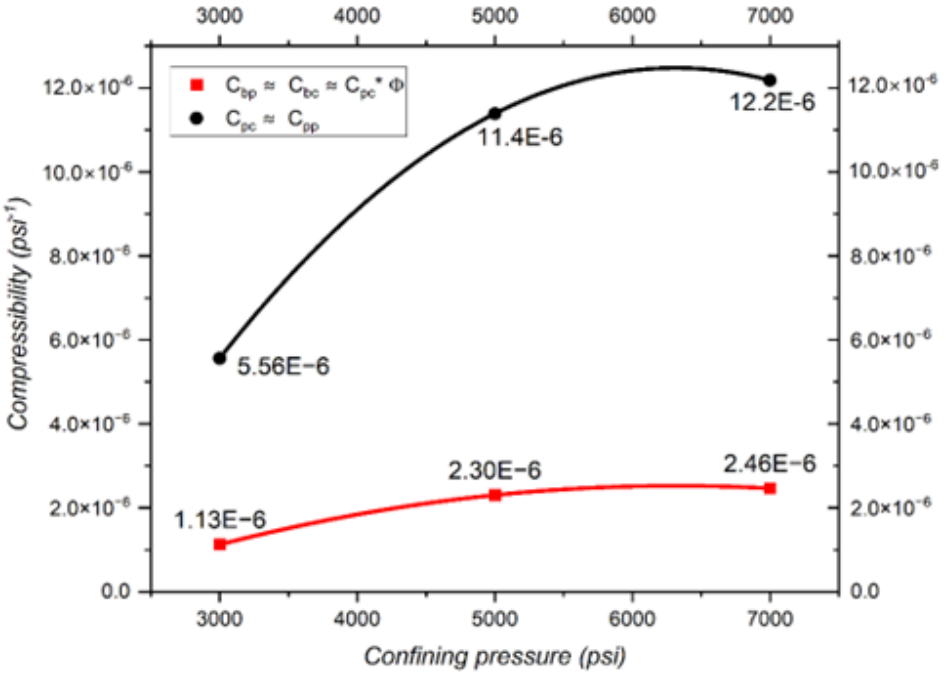

Fig. 4 - 2: Comparison of compressibilities using oil for sample F1: red curve shows the trend of bulk compressibilities, while black curve depicts the behavior of pore compressibilities.

In contrast to the trend seen in sample M3, sample F1 exhibits a distinctly different behavior regarding compressibility and effective stress. Specifically, compressibility increases with rising P_c, indicating that it grows when exposed to higher effective stress levels.

4.2 POROSITY CORRELATION MODEL

After analyzing the relationship between porosity and effective stress for both samples, the following presents the correlation between ϕ and C_{pc}. This correlation is valuable for developing an analytical model to predict the relation between these properties. To facilitate this, **Table 4 - 3** summarizes the polynomial coefficients generated for both samples, while **Figs. 4 – 3** and **4 – 4** illustrate the correlation trends.

Table 4 - 3: Polynomial coefficients correlating to compressibility and porosity.

Core	Coefficients			
	A	B	C	R-Square value R^2
M3	0.250	−0.064	0.00419	0.97
F1	−0.116	0.044	−0.00429	1

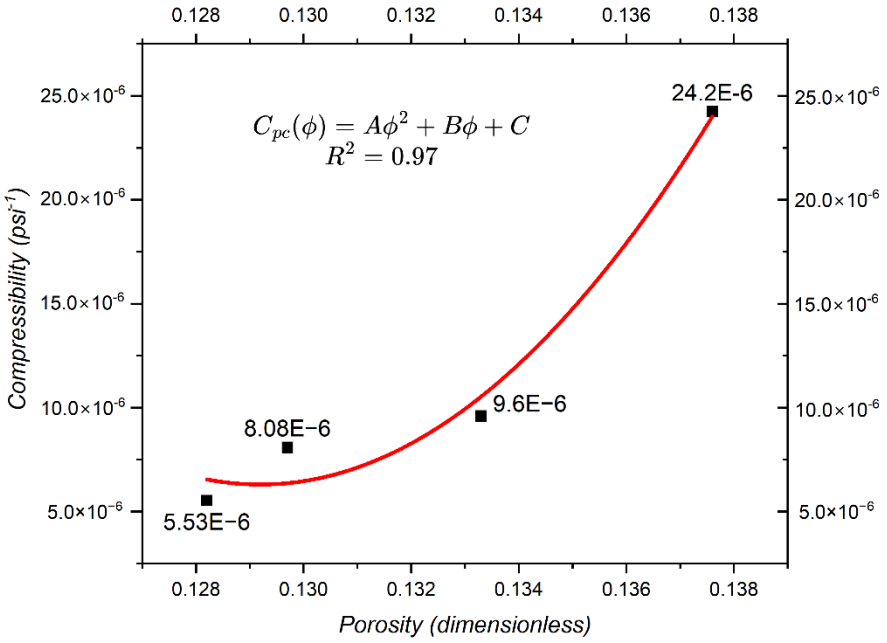

Fig. 4 - 3: Relationship between porosity and compressibility for core M3.

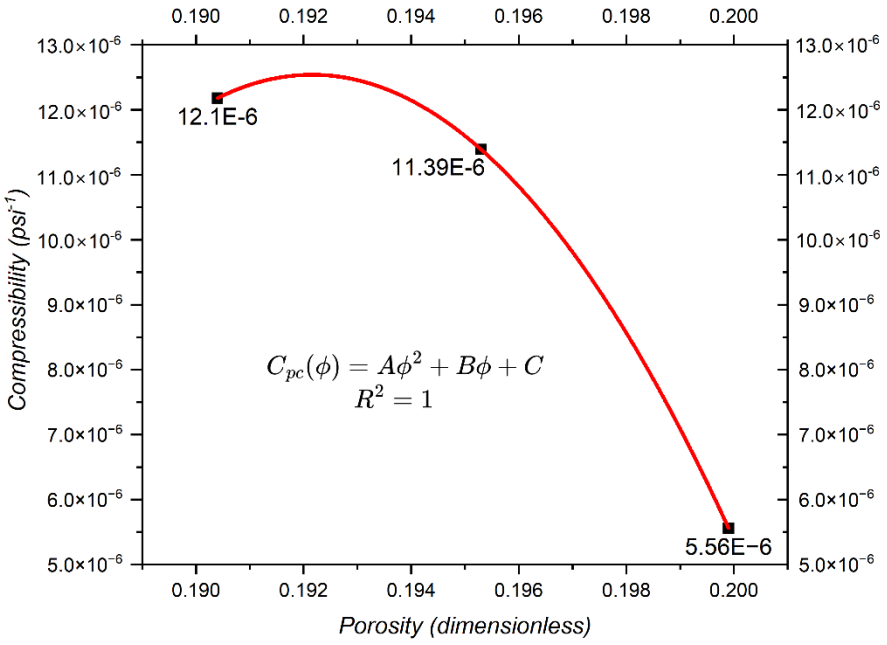

Fig. 4 - 4: Relationship between porosity and compressibility for core F1.

4.3 PERMEABILITY CORRELATION MODEL

Regarding permeability, **Table 4 - 4** presents the coefficients derived from the correlation with C_{pc}, while **Fig. 4 - 5** illustrates this relationship. It indicates that permeability remains unaffected by the unusual behavior observed in previous properties, which is linked to the inherent qualities of the k property itself.

Table 4 - 4: Polynomial coefficients correlating to compressibility and permeability for core M3.

Core	Coefficients			
	A	B	C	R-square value R^2
M3	$1.907E-9$	$-3.286E-7$	$1.964E-5$	0.942

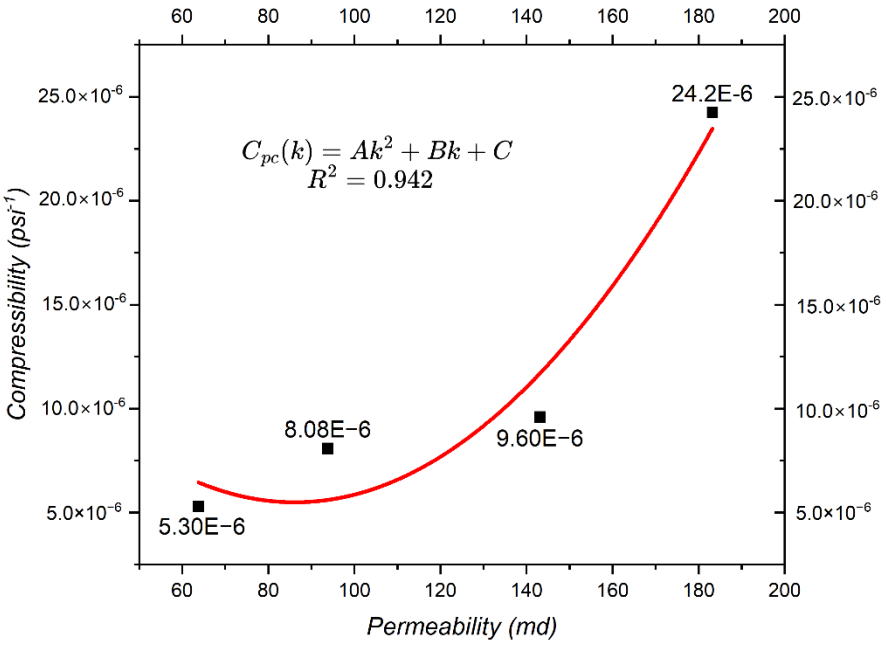

Fig. 4 - 5: Relationship between permeability and compressibility for core M3.

The outlier trends observed in sample F1 align closely with findings from other studies that report similar behaviors. For instance, in the work by Schutjens et al. (2012), while the specific trend was not explored in depth as it was not the focal point of their research, there is an evident decrement in compressibility as porosity increases in the sandstone sample examined. The authors note that this pattern is typical for well-consolidated sandstones with porosities below 20%, at least in the context of their study.

Similarly, Ganat et al. (2024) conducted an analysis of approximately 161 samples and indicated that compressibility decreases as porosity increases, which aligns with the findings presented in this study.

Finally, Unalmiser et al. (1993) conducted a study that reveals an unusual trend contrary to common expectations, as they found a decrease in compressibility linked to an increase in porosity.

While the cited studies illustrate unusual compressibility behavior related to porosity, they effectively show that the findings for sample F1 are not just an outlier but align with some established examples in literature. Considering this, several hypotheses are proposed to clarify the observations, particularly:

- At low confining pressures, the mineral grains in the sample rearrange, and upon reaching maximum P_c, a reduction in compressibility is anticipated.
- Micro-fractures emerge in the sample, leading to a rise in pore volume and, as a result, in compressibility.
- Expansion of the fluids used for pore saturation occurs, forcing sample expansion.
- Stress relaxation occurs, which leads to an uneven redistribution of P_c, resulting in localized pore expansion due to overall stress relief.

Once again, it must be emphasized that these are not definitive answers, as further studies and additional tests focusing exclusively on analyzing this behavior are necessary. Consequently, the ideas mentioned above remain purely speculative.

Moreover, **Fig. 4 - 6** illustrates the porosity, permeability, and compressibility trends in a three-dimensional diagram, offering an additional perspective on the relationships discussed in this section. These properties relate to the data collected for sample M3, which is the only sample that allowed for the examination of absolute permeability to gas.

This enables the visualization of the dependence among properties that are hard to discern in two dimensions. It enhances the assessment of functional relationships between them. It allows for the creation of models or interpolation between properties, presenting a wide array of opportunities and hidden benefits for analysis.

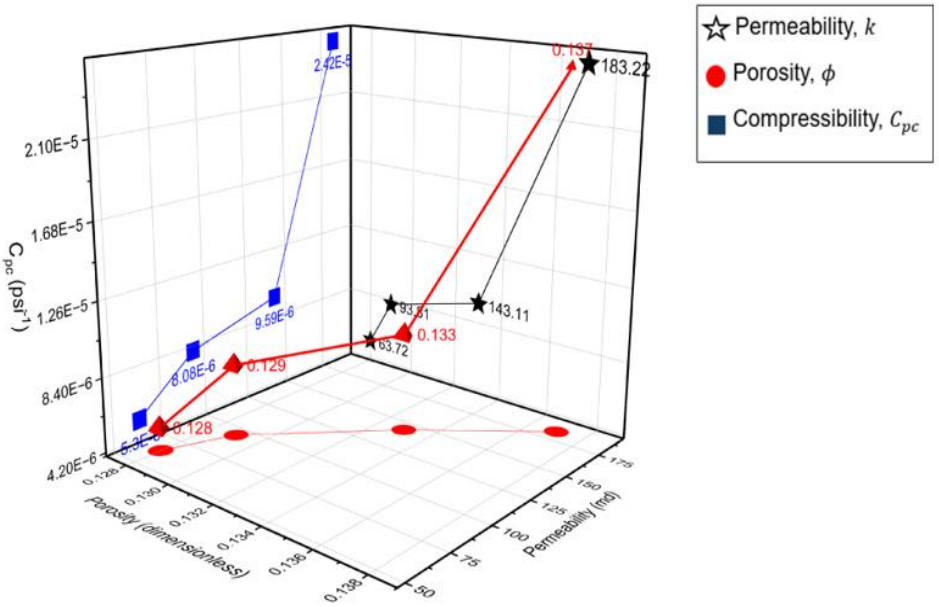

Fig. 4 - 6: 3-D diagram illustrating variable interactions in sample M3.

CHAPTER 5

5. CONSTITUTIVE BEHAVIOR

Constitutive behavior is traditionally defined as the equations that relate variables such as strain, permeability, porosity, or compressibility, among others, to describe the mechanical response of rock when subjected to various stress states.

This chapter analyzes relationships based on experimental data to characterize the cores' constitutive behavior subjected to hydrostatic stress conditions. Consequently, models are developed to connect strain with parameters measured in the laboratory, such as C_{pc}, k and ϕ.

Before discussing the proposed expressions, the compressibility equation must be revisited to link it with strain explicitly. This approach allows for estimating the volumetric strains, ε_v, in the samples caused by stress. Therefore, return to **Eq. 22** and grouping the compressibility with the partial derivative of the pressure in the first term and retaining the second term associated with the volumes results in the following expression:

$$C_{pc}(dP_c) = -dV_p/V_p^i. \tag{30}$$

Recalling **Eq. 11**, which defines volumetric strain, and combining with **Eq. 30** results in:

$$\varepsilon_v = C_{bc}dp. \tag{31}$$

The above expression enables the calculation of volumetric strain based on effective stress and volumetric compressibility C_{bc}, see **Eq. 29**. It's important to note that the negative sign typically associated with compressibility is omitted because this study assumes deformation always indicates volume decrease. This convention simplifies reading and comparing stress conditions without confusion about the direction of volumetric change, which is relevant in geomechanics contexts.

Tables 5 – 1 and **5 – 2** are presented below. They summarize the strain values for each sample and clarify that the compressibilities utilized in the calculations were derived from the oil methodology.

Plotting the relationship between P_c and ε_v reveals the usual trend: deformation increases more than previously observed as stress magnitude rises; see **Figs. 5 – 1** and **5 – 2**.

Table 5 - 1: Volumetric strain values pertaining to core M3.

Confining pressure $(\boldsymbol{P_c})$ $\boldsymbol{psi}$	**Unit volumetric strain** $(\boldsymbol{\varepsilon_v})$ $\boldsymbol{dimensionless}$
$\mathbf{1000}$	0
$\mathbf{4000}$	0.01000
$\mathbf{7000}$	0.01384
$\mathbf{10,000}$	0.01699
$\mathbf{12,000}$	0.01835

Table 5 - 2: Volumetric strain values pertaining to core F1**.**

Confining pressure $(\boldsymbol{P_c})$ $\boldsymbol{psi}$	**Unit volumetric strain** $(\boldsymbol{\varepsilon_v})$ $\boldsymbol{dimensionless}$
$\mathbf{1000}$	0
$\mathbf{3000}$	0.00225
$\mathbf{5000}$	0.00685
$\mathbf{7000}$	0.01178

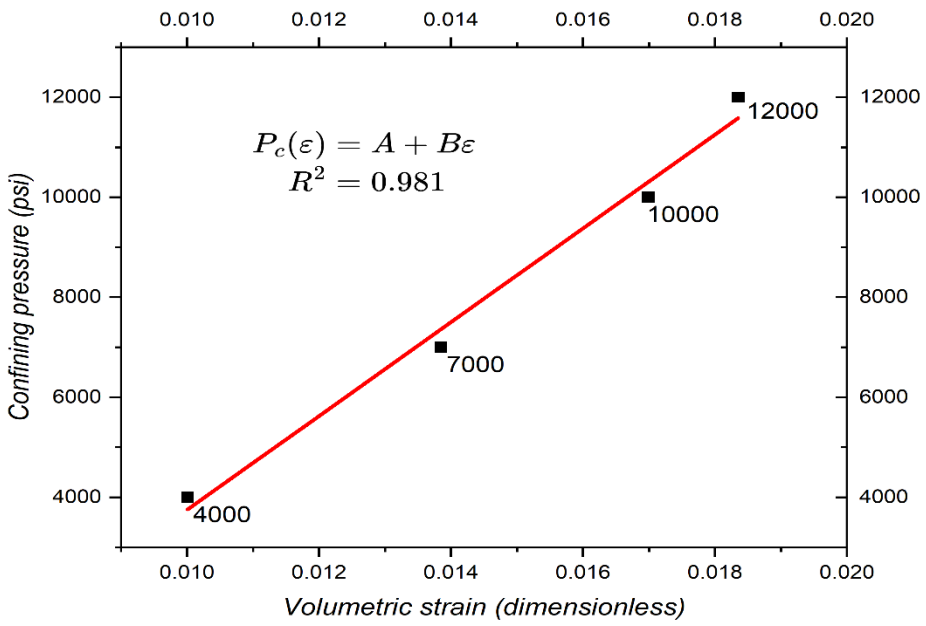

Fig. 5 - 1: Trend of confining pressure as a function of volumetric strain for sample M3.

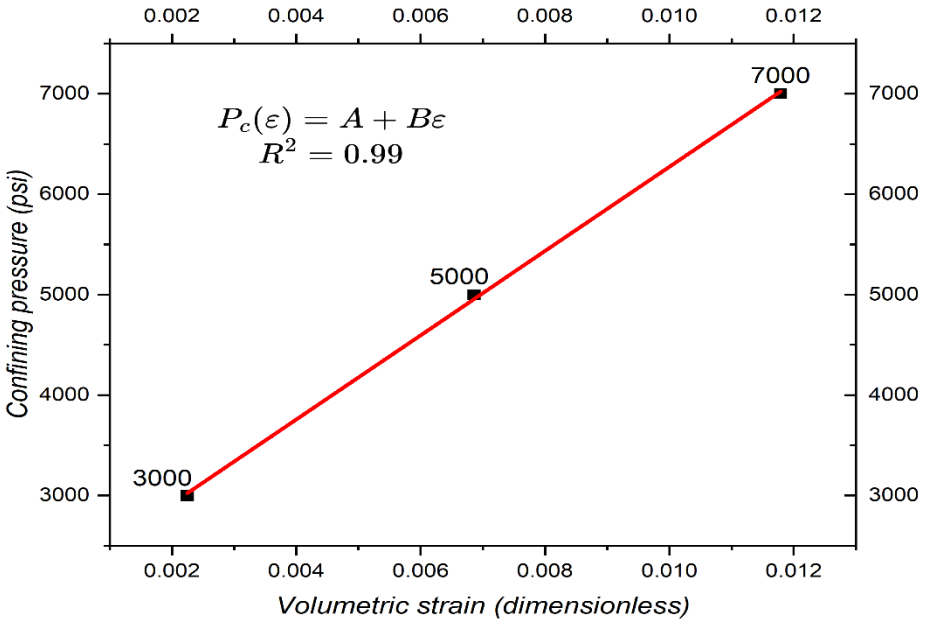

Fig. 5 - 2: Trend of confining pressure as a function of volumetric strain for sample F1.

Upon closer examination, it becomes evident that a significant increase in ε_s is attributed to elevated levels of effective stress. In other words, the specimens exhibit more pronounced strain under high confining pressures. **Table 5 - 3** displays the coefficients of the lines shown in the prior graphs.

5.1 CONSTITUTIVE BEHAVIOR OF VOLUMETRIC STRAIN AND POROSITY

After reporting the porosity and volumetric strain data for both samples, the following step is to create a graphical representation that illustrates the relationship between the variables. This will facilitate the development of a model that accurately reflects the constitutive relationship. As demonstrated below, a linear model emerged as the best fit and was utilized for most properties.

Figs. 5 – 3 and **5 – 4** show the behavior between porosity and volumetric strain.

Table 5 - 3: Linear coefficients generated for P_c and ε_v.

Core	A	B	R-square value R^2
M3	-5625.846	937642.32	0.981
F1	2079.75	419243.83	0.999

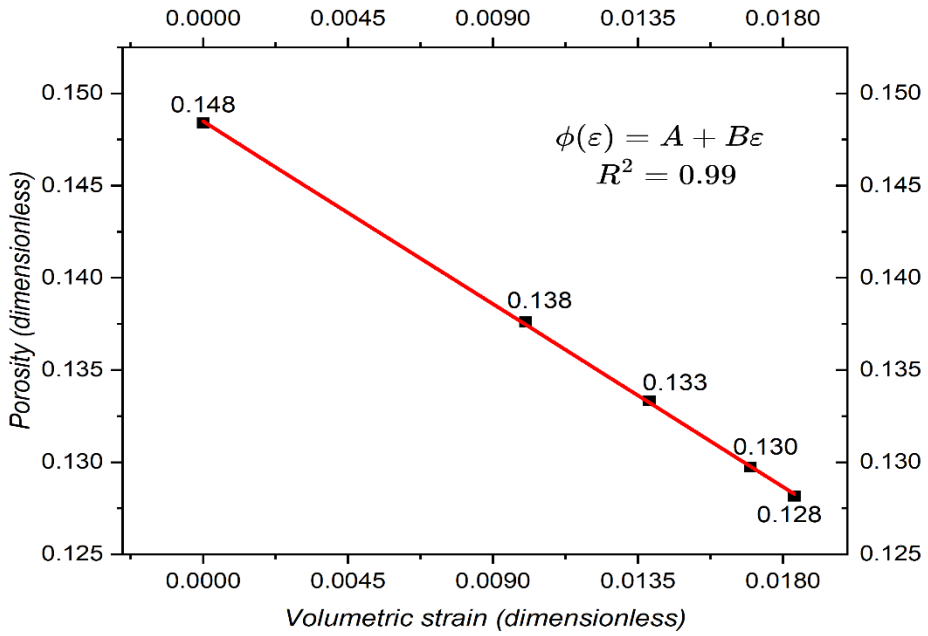

Fig. 5 - 3: Constitutive behavior relating volumetric strain to porosity for sample M3.

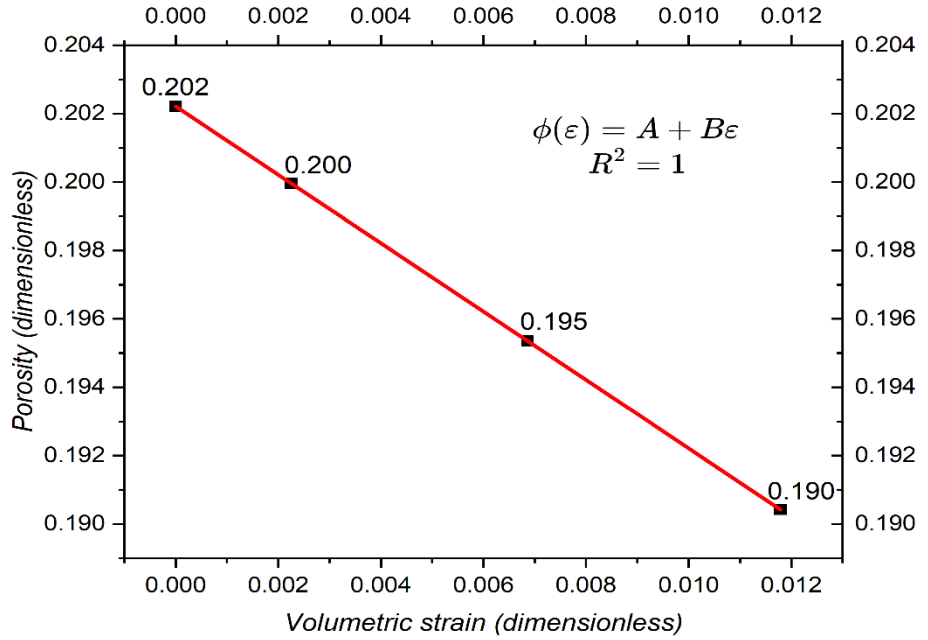

Fig. 5 - 4: Constitutive behavior relating volumetric strain to porosity for sample F1.

Table 5 - 4: Linear coefficients generated for ϕ and ε_v.

Core	A	B	R-square value R^2
M3	0.14848	-1.1011	0.999
F1	0.02022	-1	1

The behavior observed in both samples aligns with expectations. As deformation in the rock pores—especially sensitive to stress loading—increases, the volume decreases. This is related to the compressibility of V_p, resulting in granular reorganization and potentially even the pores' collapse.

Above is **Table 5 - 4**, which outlines the value of the coefficients from the previously discussed models.

5.2 CONSTITUTIVE BEHAVIOR OF VOLUMETRIC STRAIN AND PERMEABILITY

As anticipated, a relationship between the calculated strain and the absolute gas permeability for sample M3 was successfully established, revealing a significant correlation in these two variables. The quadratic fit of the observed behavior, a criterion consistently applied in all the developed expressions, resulted with high accuracy of approximately $R^2 = 0.97$.

Therefore, **Fig. 5 - 5** illustrates the relationship between deformation and permeability, while **Table 5 - 5** provides detailed values of the coefficients in the derived expression.

In the figure, it is evident that an increase in the deformation of the sample results in a decrease in permeability values. This reduction indicates that the effects related to the deformation of the rock are intensified, leading to a decrease in pore volume, particularly within those that are hydraulically connected (effective porosity). Consequently, the movement of fluid through the rock is impeded. When applied to

the exploitation of a field, this phenomenon signifies a decline in productivity as the stress increases, which ultimately translates into economic losses.

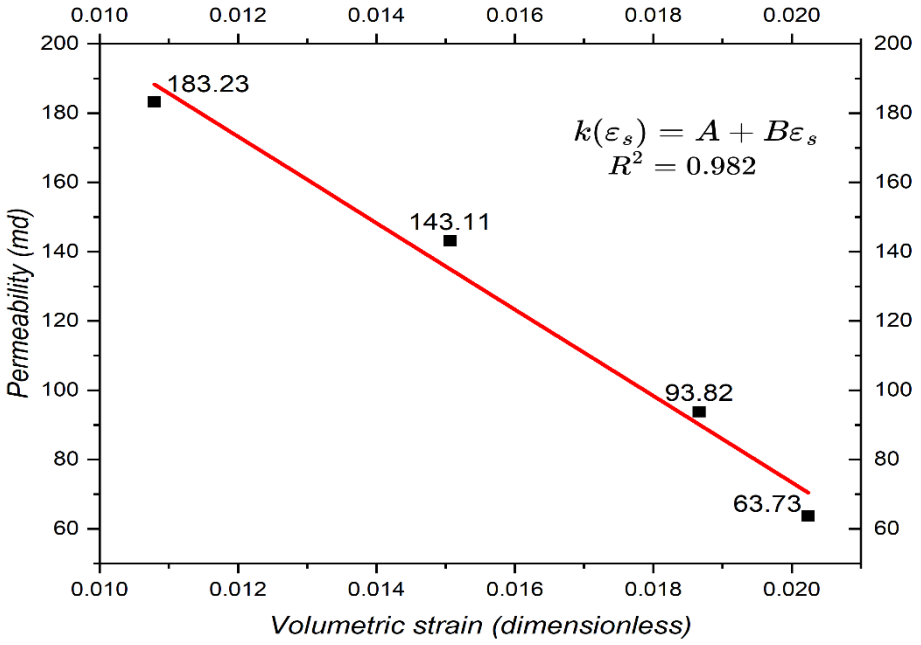

Fig. 5 - 5: Constitutive behavior relating volumetric strain to permeability for sample M3.

Table 5 - 5: Constitutive model coefficients between k and ε_v for sample M3.

Core	A	B	R-square value R^2
M3	322.926	−12475.049	0.982

5.3 CONSTITUTIVE BEHAVIOR OF VOLUMETRIC STRAIN AND COMPRESSIBILITY

Ultimately, concerning the constitutive behaviors, it is imperative to correlate compressibility c_{bc} and volumetric strain ε_s to provide insight into the evolution of the rocks' mechanical response as the stress increases.

In contrast, the models introduced in this section adopt a different approach from those used earlier. They failed to achieve an acceptable tolerance, prompting a search for alternatives that could ensure it.

Fig. 5 - 6 illustrate the trend for the core M3; the exponential model was identified as the best fit for behavior. The generated trend aligns with expectations, as increased strains lead to a decrease in compressibility. This happens because the rock's porous system is progressively reduced, resulting in less volume available for deformation.

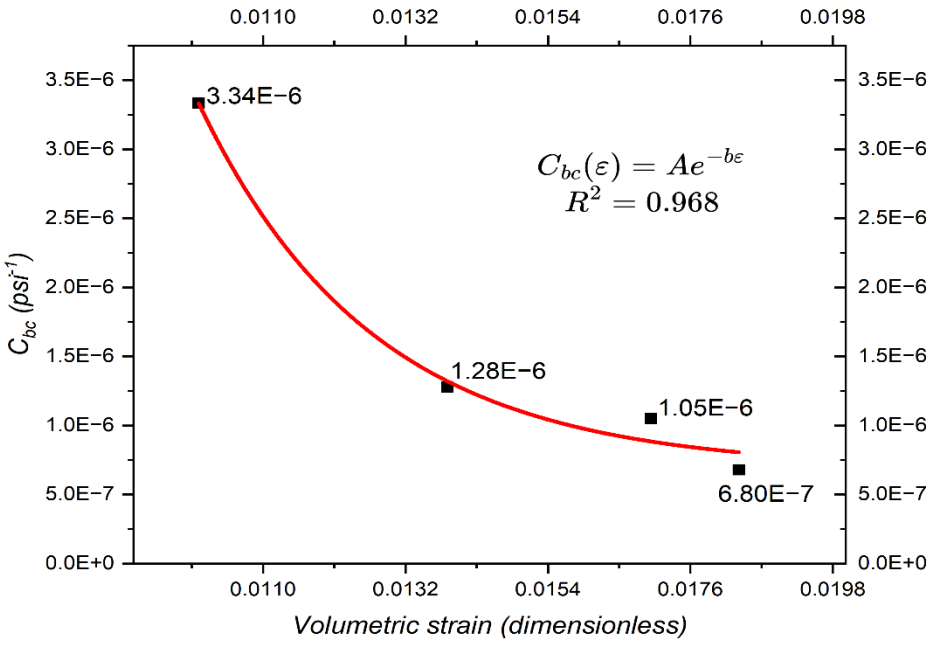

Fig. 5 - 6: Mechanical behavior of core M3 as a function of C_{bc} y ε_v.

Conversely, **Fig. 5 - 7** shows the trend for sample F1, the most suitable model is a logarithmic one. However, like the analysis of C_{pc} as a function of P_c, it shows distinct singularities, as increased strain increases compressibility. This observation reaffirms the previous chapter's insights regarding the trends; the irregular behavior possibly indicates that high stresses lead to irregular mechanical behavior.

The coefficients of these models for both samples are presented in **Table 5 - 6**.

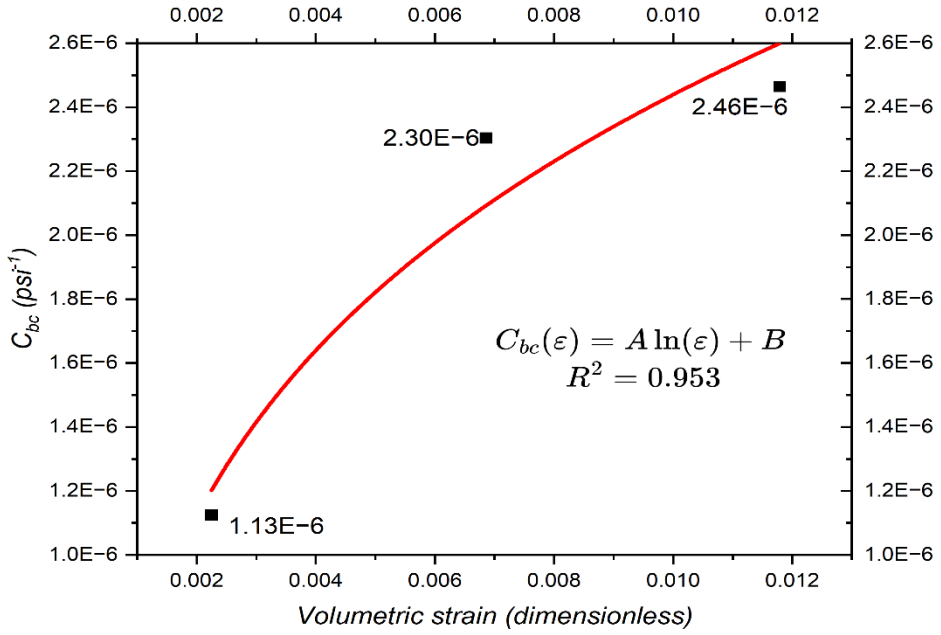

Fig. 5 - 7: Mechanical behavior of core F1 as a function of C_{bc} y ε_v.

Table 5 - 6: Coefficients of the exponential model for sample M3 and the logarithmic model for sample F1.

Core	A	B	R-square value R^2
M3	$1.792x10^{-5}$	-176.2	0.968
F1	$8x10^{-7}$	$6x10^{-6}$	0.953

5.4 ELASTIC MODULUS

This section outlines several mechanical properties estimated from the experimental data, which are discussed in greater detail in **Appendix B** at the end of this document.

These elastic constants, also known as elastic modulus, are named for their ability to describe the material's properties as it experiences stress, deforms, and then returns to its original shape once the stress is removed, as stated in the Energy Glossary SLB.

5.4.1 BULK MODULUS

To compute the bulk modulus, **Eq. 32** was employed, which relates to the inverse of c_{bc}. **Tables 5 – 7** and **5 – 8** detail the values as a function of the effective stress for each sample. Notably, this modulus is conventionally denoted by the letter K; for practicality, the same notation will be utilized in this work. This specification seeks to preclude any potential confusion with permeability, which is similarly represented by the letter k, albeit in lowercase.

$$K = 1/C_{bc}, \tag{32}$$

where:

K: Bulk modulus [psi].

Table 5 - 7: Estimated values of the bulk modulus for core M3.

Confining pressure (P_c) psi	**Bulk modulus** (K) psi
4000	$3x10^5$
7000	$7.82x10^5$
10,000	$9.54x10^5$
12,000	$1.47x10^6$

Table 5 - 8: Estimated values of the bulk modulus for core F1.

Confining pressure (P_c) psi	Bulk modulus (K) psi
3000	$8.89x10^5$
5000	$4.34x10^5$
7000	$4.06x10^5$

The behavior of the bulk modulus as a function of confining pressure is illustrated below. The exact modeling approximation was applied to both samples. **Fig. 5 - 8** represents sample M3, a positive correlation is noted: as the stress rises, the modulus K also increases. This indicates that the applied pressure makes the rock progressively more resistant to deformation or compression.

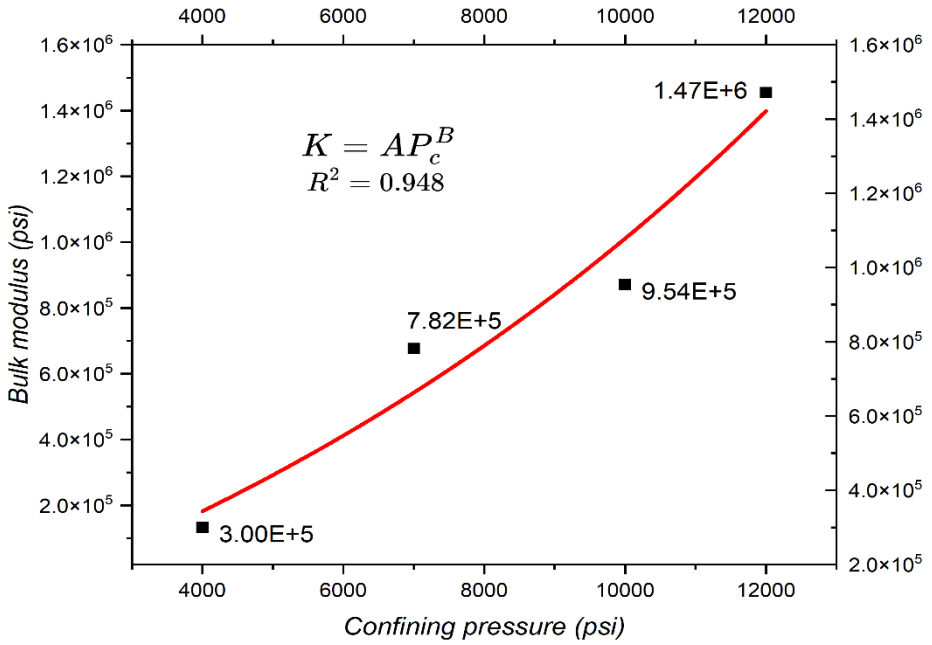

Fig. 5 - 8: Mechanical response of modulus K as a function of confining pressure for sample M3.

Fig. 5 - 9, which illustrates the correlation between K modulus and applied stress for sample F1, a distinctly different trend emerges compared to earlier observations. This connects to ongoing discussions animated by unique characteristics noted during analyzing its petrophysical and mechanical properties.

In this trend, it is observed that the grains of the material do not entirely regroup, resulting in a decrease in the K modulus, which is associated with the ongoing deformation phenomenon.

Table 5 − 9 presents the coefficients for the expressions, indicating that the fit for these models was exponential in both instances.

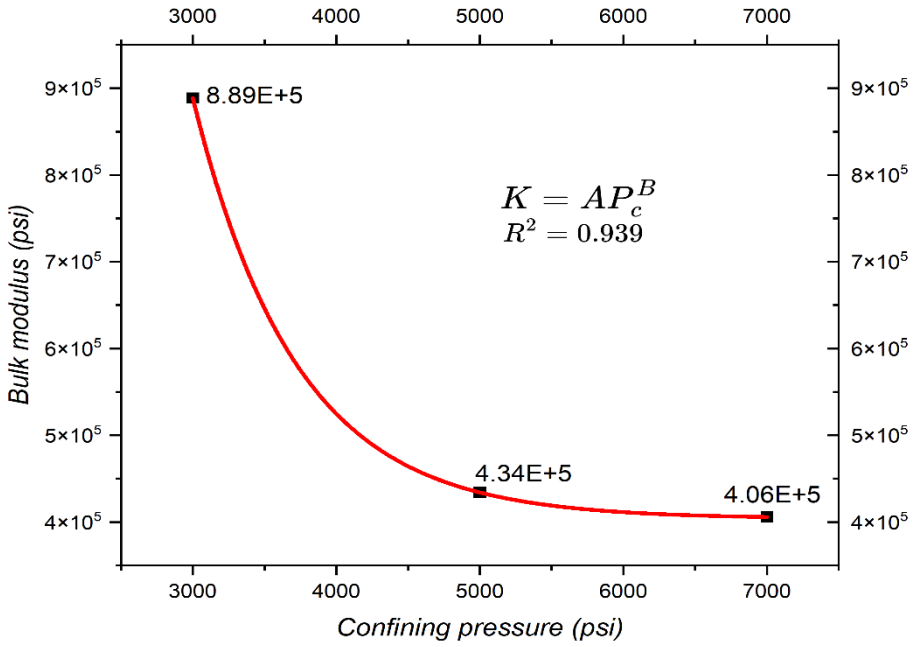

Fig. 5 - 9: Mechanical response of modulus K as a function of confining pressure for sample F1.

Table 5 – 9: Exponential fit coefficients of the bulk modulus for samples.

Core	A	B	R-square value R^2
$M3$	3.8198	1.3647	0.948
$F1$	$1.88x10^9$	−0.964	0.939

5.4.2 YOUNG'S MODULUS

Utilizing **Eq. 33** allows for estimating values of the modulus of elasticity.

$$E = 3K(1 - 2v), \tag{33}$$

in which:

E: Young's modulus $[psi]$.

v: Poisson's ratio $[dimensionless]$.

To use this expression, knowledge of Poisson's ratio is essential, which is derived only under axial stress. Based on Zoback (2007), for a high porosity sandstone like the samples in this study, a Poisson's coefficient of about $v = 0.20$ is suggested. This facilitates the calculation of any mechanical property related to this coefficient.

Tables 5 – 10 and **5 – 11** provide a summary of the calculated Young's modulus E values for each sample.

Table 5 - 10: Estimated values of the Young's modulus (E) for core M3.

Confining pressure (P_c) psi	**Young's modulus** (E) psi
1000	–
4000	$5.3959x10^5$
7000	$1.4069x10^6$
10,000	$1.7170x10^6$
12,000	$2.6485x10^6$

Table 5 - 11: Estimated values of the Young's modulus (E) for core F1.

Confining pressure (P_c) psi	**Young's modulus** (E) psi
1000	–
3000	$1.60x10^6$
5000	$7.8126x10^5$
7000	$7.3031x10^5$

The relationship between Young's modulus and effective stress is illustrated. In **Fig. 5 - 10**; the trend for sample M3 aligns with previous analyses, as the E modulus rises with increasing effective stress, suggesting the rock's internal structure becomes more rigid.

Conversely, **Fig. 5 - 11** illustrates that the observed trend diverges from those above, indicating a decrease in the E modulus. The graphs suggest that the trend begins with non-linear, or even inelastic, behavior, possibly due to the atypical characteristics of the sample. This is evidenced by a lighter increase in V_p and ϕ—likely caused by mineral reorganization—which are properties that significantly influence E modulus in porous rocks.

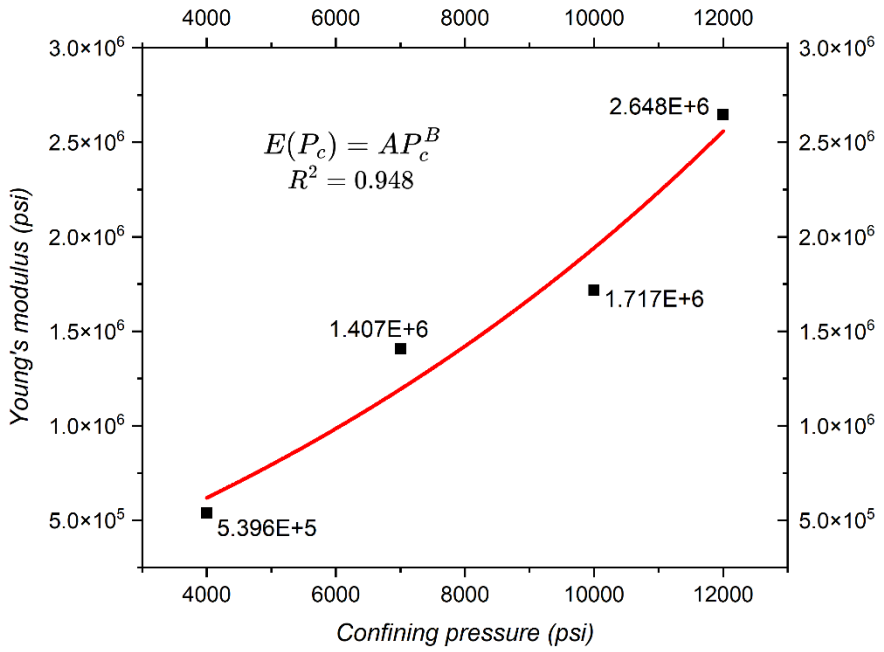

Fig. 5 - 10: Mechanical response of the Young's modulus E as a function of confining pressure for sample M3.

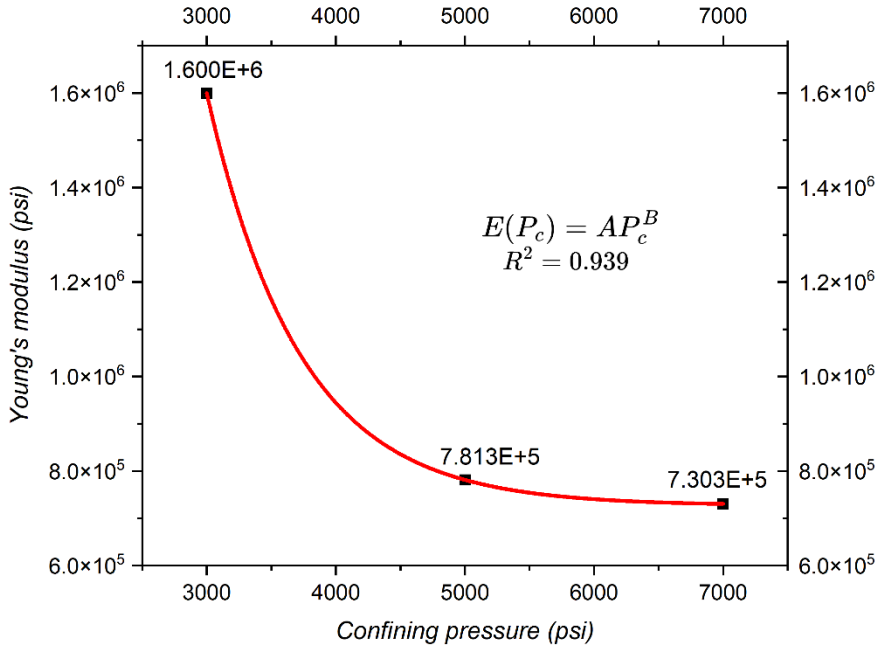

Fig. 5 - 11: Mechanical response of the Young's modulus E as a function of confining pressure for sample F1.

Table 5 - 12 presents the coefficients of potential adjustments utilized in both samples.

Table 5 - 12: Exponential fit coefficients of the Young's modulus for samples.

Core	A	B	R-square value R^2
M3	6.8756	1.3647	0.94
F1	$3x10^9$	-0.964	0.93

5.4.3 SHEAR MODULUS

This modulus is one of the two Lame constants. It was derived from the formula in **Eq. 34**, which necessitated only the modulus of elasticity E and the proposed Poisson ratio v. Consequently, **Tables 5 – 13** and **5 – 14** compile the results.

$$G = E/(2 + 2v), \tag{34}$$

with:

G: Shear modulus $[psi]$.

Table 5 - 13: Estimated values of the shear modulus for core M3.

Confining pressure (P_c) psi	Shear modulus(G) psi
$\mathbf{1000}$	$-$
$\mathbf{4000}$	$2.2483x10^5$
$\mathbf{7000}$	$5.8619x10^5$
$\mathbf{10,000}$	$7.1540x10^5$
$\mathbf{12,000}$	$1.1035x10^6$

Table 5 - 14: Estimated values of the shear modulus for core F1.

Confining pressure (P_c) psi	**Shear modulus** (G) psi
1000	–
3000	$6.6655x10^5$
5000	$3.2552x10^5$
7000	$3.0429x10^5$

In summary, the trends produced for this modulus as a function of the effective stress are illustrated. **Fig. 5 - 12** depicts the mechanical behavior of core M3, showing a positive trend, indicating a directly proportional relationship.

However, **Fig. 5 - 13** illustrates the relationship between the modulus G and the effective stress for sample F1; a distinct behavior is observed: the modulus G diminishes as P_c rises, indicating that the rock remains unaffected and undistorted by the shear stresses that may be induced.

Nonetheless, the ratio of coefficients in the previous trends noted is presented in **Table 5 - 15** below.

Table 5 - 15: Exponential fit coefficients of the shear modulus for the samples.

Core	**A**	**B**	**R-value square** R^2
$M3$	2.8648	1.3647	0.94
$F1$	$1.41x10^9$	-0.964	0.93

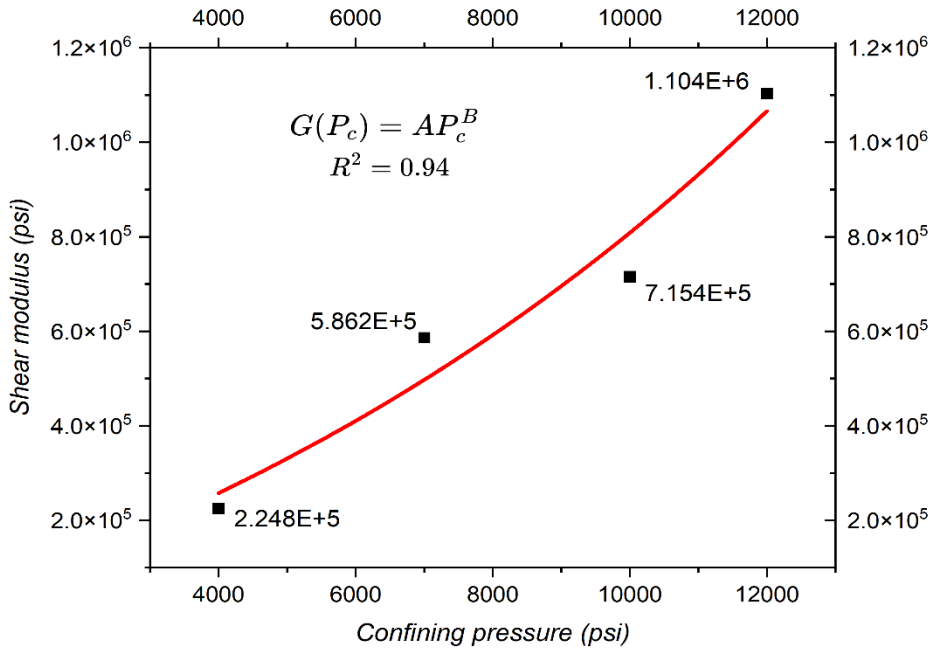

Fig. 5 - 12: Mechanical response of the shear modulus G as a function of confining pressure for sample M3.

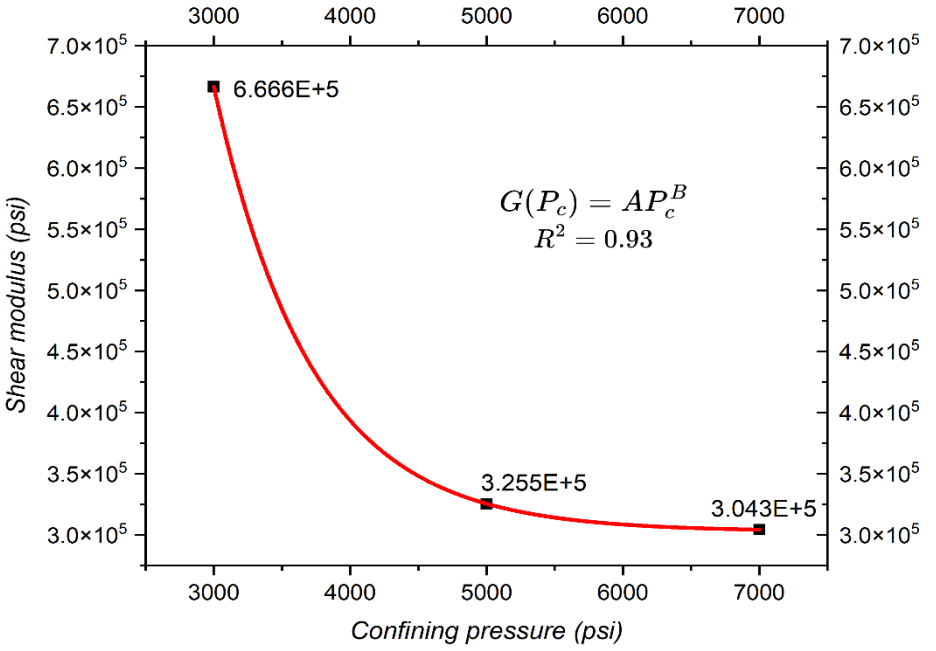

Fig. 5 - 13: Mechanical response of the shear modulus G as a function of confining pressure for sample F1.

5.4.4 LAMÉ CONSTANT

In conclusion of this section, the final elastic constant determined in this experiment, known as the Lamé constant λ, is presented. It is important to note that this constant cannot be easily interpreted in physical terms; however, in conjunction with the shear modulus G, it describes the mechanical behavior of an isotropic and elastic material within the framework of the linear elasticity theory.

Therefore, by utilizing **Eq. 35** and other elastic moduli, it became feasible to estimate λ, which is detailed in **Tables 5 – 16** and **5 – 17**. Subsequently, **Figs 5 – 14** and **5 – 15** illustrate how this parameter behaves mechanically to the effective stress.

$$\lambda = K - (2/3)\, G, \tag{35}$$

where:

λ: Lamé constant [psi].

Table 5 - 16: Estimated values of the Lamé constant (λ) for core M3.

Confining pressure (P_c) psi	**Lamé constant** (λ) psi
1000	–
4000	$1.499x10^5$
7000	$3.908x10^5$
10,000	$4.769x10^5$
12,000	$7.357x10^5$

Table 5 - 17: Estimated values of the Lamé constant (λ) for core F1.

Confining pressure (P_c) psi	Lamé constant (λ) psi
1000	–
3000	$4.4437x10^5$
5000	$2.1702x10^5$
7000	$2.029x10^5$

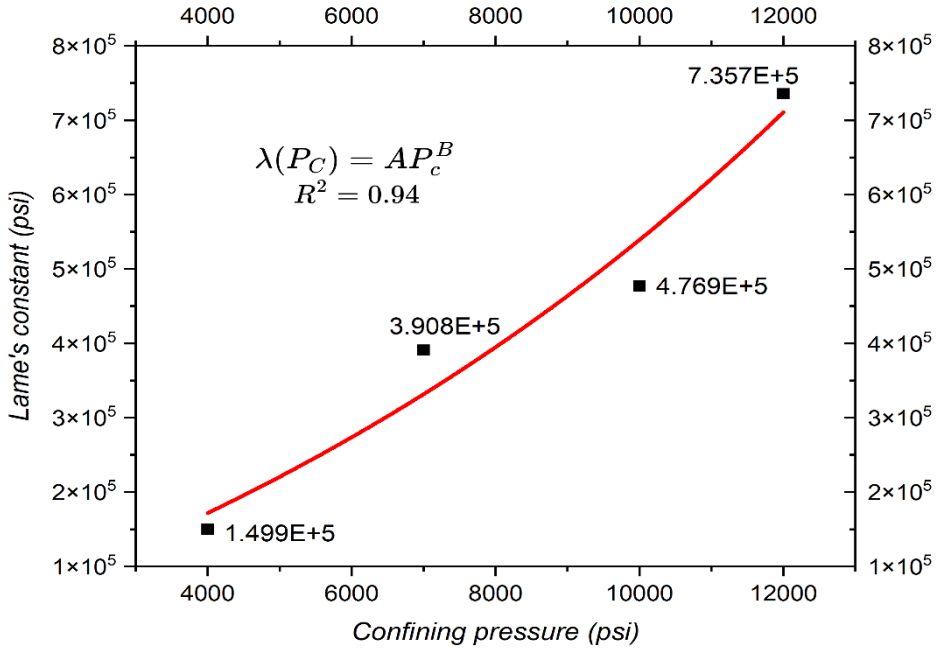

Fig. 5 - 14: Mechanical response of the Lamé constant λ as a function of confining pressure for sample M3.

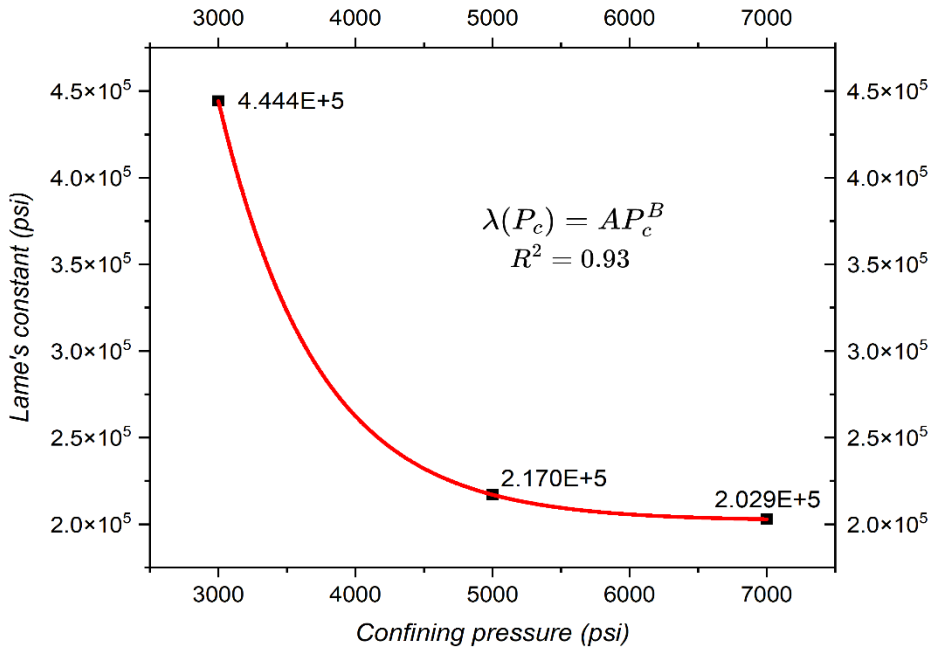

Fig. 5 - 15: Mechanical response of the Lamé constant λ as a function of confining pressure for sample F1.

Table 5 - 18 presents the coefficients of the exponential fit applied to the trends generated.

Table 5 - 18: Exponential fit coefficients of the shear modulus for the samples.

Core	A	B	R-square value R^2
M3	1.9099	1.3647	0.948
F1	$9.40x10^8$	−0.964	0.939

CHAPTER 6

6. GENERAL CONCLUSIONS

The ongoing research successfully fulfills its initial goals and objectives. It developed a methodology to determine the reservoir's compressibility at pressures around 12,000 psi and average temperatures of 150 °C. Furthermore, this research derived correlations between the measured properties, establishing a functional relation with the constitutive behavior of the samples used and estimating some of their elastic modulus. These outstanding results are significant achievements of this thesis.

The primary conclusions of this study are outlined below, followed by a series of recommendations intended to guide future research endeavors. It is essential to emphasize that this work functions as a preliminary framework that can be elaborated upon through subsequent investigations.

Key achievements:

- An experimental methodology has emerged as innovative when contrasted with the international research documented to support this study.
- Full-diameter samples were utilized, providing greater depth and representativeness for the results.
- Exposing the samples to higher pressure and temperature conditions overcomes some limitations faced in earlier years, when operational conditions were usually typical laboratory settings.
- Around eight unique correlations were created and examined for each sample. These correlations highlighted key physical properties under conditions similar to those in reservoirs.
- These correlations delineate the interrelation between petrophysical and mechanical properties, thereby accurately characterizing the constitutive behavior of the rocks.

- Experimental data reliably estimated elastic moduli, showing that it is feasible to infer important geomechanical properties through petrophysical measurements.
- The integration of petrophysical and geomechanical testing was demonstrated to markedly reduce experimental costs and time associated with experimental studies, without sacrificing data quality.

Recommendations:

- The experiment should extend the tests on sandstones by including saturation conditions typical of the reservoirs where the samples come from, such as oil, connate water, and gas, rather than using mineral oils.
- Once the sandstone tests have been completed, it is proposed to explore the utilization of more complex lithologies, such as those exhibiting double porosity or naturally fractured characteristics, given that the country possesses a substantial proportion of such reservoirs.

BIBLIOGRAPHY

Andersen, M. A. 1988. Predicting Reservoir-Condition PV Compressibility from Hydrostatic-Stress Laboratory Data. *SPE Res Eng* ***3*** (03): 1078–1082. SPE-14213-PA. https://doi.org/10.2118/14213-PA

Cabrera, D. and Samaniego, F. 2022. Experimental Mechanics of Fractured Porous Rocks. In *Petrophysical Classification of Rocks,* ed. Springer, Chap. 2, 9–20.

Darcy, H. 1856. *Les Fontaines Publiques de la Ville de Dijon*. Hendrik Conscience Heritage Library, Paris, France.

de Oliveira, G. L., Ceia, M. A., Missagia, R. M. et al. 2016. Pore Volume Compressibilities of Sandstones and Carbonates from Helium Porosimetry Measurements. *Journal of Petroleum Science and Engineering* ***137***, 185–201 (January). https://doi.org/10.1016/j.petrol.2015.11.022

de Siqueira., Silva, F., Marsili., et. al. 2018. Estimation of Permeability, Porosity and Rock Compressibility Properties using Digital Rock Analysis Technique for a Heavy Oil Unconsolidated Sandstone Offshore Brazil. Presented at the AAPG 2018 Annual Convention & Exhibition, Salt Lake City, Utah, United States, 20–23 May. https://doi.org/10.1306/30587deSiqueira2018

Dobrynin, V. M. 1962. Effect Of Overburden Pressure on Some Properties of Sandstones. *SPE J* **2** (04): 360–366. SPE-461-PA. https://doi.org/10.2118/461-PA

Energy Glossary SLB. 1998. Elastic Constants, elastic constants | Energy Glossary (accessed 12 April 2025).

Fatt, I. 1958. Pore Volume Compressibilities of Sandstone Reservoir Rocks. *J Pet Technol* **10** (1958): 64–66, (March). https://doi.org/10.2118/970-G

Gallardo, E. H. 2023. Dictámenes Técnicos al Plan de Desarrollo para la Extracción. Final report, Assignment A-0375-3M-Campo Zaap, CNH, México (September)

Ganat, T., Hrairi, M., Badawy, A. et al. 2024. Advancing Sandstone Reservoir Compressibility Prediction: A Correlation-Driven Methodology. *Petroleum Research*, **9**(2), 273–279 (June). https://doi.org/10.1016/j.ptlrs.2024.01.006

Geertsma, J. 1957. The Effect of Fluid Pressure Decline on Volumetric Changes of Porous Rocks. *Transactions of the AIME* **210** (01): 331–340, (December). https://doi.org/10.2118/728-G

Hall, H. N. 1953. Compressibility of Reservoir Rocks. *J Pet Technol* **5** (01): 17–19, (January). https://doi.org/10.2118/953309-G

Jaeger, J. C., Cook, W., and Zimmerman, R. 2007. Fundamentals of Rock Mechanics. In *Poroelasticity and Thermoelasticity,* ed. Blackwell, Chap. 7, 168–197.

Jalalh, A. 2006. Compressibility of porous rocks: Part II. New relationships. *Acta Geophysica* **54** (4), 399–412, (December). https://doi.org/10.2478/s11600-006-0029-4

Jha, B., Bottazzi, F., Wojcik, R., et. al. 2015. Reservoir characterization in an underground gas storage field using joint inversion of flow and geodetic data. *International Journal for Numerical and Analytical Methods in Geomechanics* ***39*** (14): 1619-1638. https://doi.org/10.1002/nag.2427

Liu, C. H., Pan, Y. W., Liao, J. J. et al. 2004. Estimating Coefficients of Volume Compressibility from Compression of Strata and Piezometric Changes in A Multiaquifer System in West Taiwan. *Engineering Geology*, **75**(1), 33–47 (September). https://doi.org/10.1016/j.enggeo.2004.04.007

Makhnenko, R. and Labuz, J. 2013. Unjacketed bulk compressibility of sandstone in laboratory experiments. Paper presented at the Poromechanics V: Proceedings of the Fifth Biot Conference on Poromechanics, Vienna, Austria, 10–12 July. https://doi.org/10.1061/9780784412992.057

McLatchie, A., Hemstock, A., and Young, W. 1958. The effective compressibility of reservoir rock and its effects on permeability. *J Pet Technol* ***10*** (06): 49–51, (June). https://doi.org/10.2118/894-G

Moosavi, S.A., Goshtasbi, K., Kazemzadeh, E. et al. 2014. Relationship Between Porosity and Permeability with Stress Using Pore Volume Compressibility Characteristic of Reservoir Rocks. *Arabian Journal of Geosciences* **7**, 231–239. https://doi.org/10.1007/s12517-012-0760-x

Newman, G. H. 1973. Pore-Volume Compressibility of Consolidated, Friable, And Unconsolidated Reservoir Rocks Under Hydrostatic Loading. *J Pet Technol* **25** (02): 129–134, (February). https://doi.org/10.2118/3835-PA

Nelson, P. H., and Batzle, M. L. 2006. Petroleum Engineering Handbook Volume I: General Engineering. In *Single-Phase Permeability*, 2ed. Society of Petroleum Engineers, Chap. 14, 687–726.

Paredes, D. A. 2023. Dictamen Técnico de la modificación al Plan de Desarrollo para la Extracción de Hidrocarburos. Final report, Contract CNH-M1-EK-BALAM/2017, CNH, México (August).

Petrakov, D., Penkov, M., and Zolotukhin, B. 2022. Experimental study on the effect of rock pressure on sandstone permeability. *Journal of Mining Institute* ***254***: 244–251. https://doi.org/10.31897/PMI.2022.24

Rodney, C. A., Estrada, C. A., Amador, J. M. et al. 2019. *Propuesta De Curvas Tipo Para Estimar Compresibilidades Del Sistema Roca-Fluido.* Petroquimex: La revista de la Industria Energética, (June). https://petroquimex.com/propuesta-de-curvas-tipo-para-estimar-compresibilidades-del-sistema-roca-fluido/

Romero, R. A. 2014. *Análisis De Incertidumbre Y Factibilidad De Inyección De Fluidos En El Campo Ogarrio, Bloque A*. MS Thesis, Facultad de Ingeniería, Universidad Nacional Autónoma de México.

Sampath, K. 1982. A New Method to Measure Pore Volume Compressibility of Sandstones. *J Pet Technol* ***34*** (06): 1360–1362, (June). https://doi.org/10.2118/10545-PA

Schutjens, P., and Heidug, W. 2012. On The Pore Volume Compressibility and Its Application as a Petrophysical Parameter. Paper presented at the 9th Biennial

International Conference & Exposition on Petroleum Geophysics, Hyderabad, Bangalore, India, 16–18 February. https://spgindia.org/spg_2012/spgp512.pdf

Settari, A. 2002. Reservoir Compaction. *J Pet Technol* **54** (08): 62–69, (August). https://doi.org/10.2118/76805-JPT

Shafer, J., Boitnott, G., and Ewy, R. 2008. Effective Stress Laws for Petrophysical Rock Properties. Presented at the SPWLA 49th Annual Logging Symposium, Austin, Texas, 25–28 May. https://onepetro.org/SPWLAALS/proceedings-abstract/SPWLA08/All-SPWLA08/27610

Suleen, F., Urbanczyk, C., and Williams, G. 2017. Design And Interpretation of An Interference Test for Determination of Formation Compressibility in A Deepwater Reservoir. Presented at the SPE Western Regional Meeting, Bakersfield, California, 23–27 April. SPE-185683-MS. https://doi.org/10.2118/185683-MS

Terzaghi, K. 1936. The Shearing Resistance of Saturated Soils and The Angle Between the Planes of Shear. Presented at the First International Conference on Soil Mechanics, Harvard University Press, Cambridge, MA. https://www.issmge.org/uploads/publications/1/44/1936_01_0017.pdf

Unalmiser, S. and Swalwell, T. 1993. Routine Determination of Pore Compressibility at Any Pressure. *Society of Core Analysis Conference paper **9317**.* Routine Determination of Pore Compressibility at Any Pressure Based on Two Point Measurements

Zhang, R., Ning, Z., Yang, F., et al. 2016. A Laboratory Study of The Porosity-Permeability Relationships of Shale and Sandstone Under Effective Stress. *International Journal of Rock Mechanics and Mining Sciences* **81**: 19–27 January. https://doi.org/10.1016/j.ijrmms.2015.11.006

Zimmerman, R. W. 1991. Compressibility of Sandstones. In *Part One: Compressibility and Stress*, Chap. 1, 8–14. California: Elsevier.

Zoback, D. M. 2007. Reservoir Geomechanics. In *Basic Constitutive Laws*, Chap. 3, 56-83. Cambridge.

APPENDIX A

Various studies indicate that the four definitions of compressibility for a porous medium may not be independent, making it possible to connect them through pore−elasticity theory.

To demonstrate their relationship, it's essential to outline the conditions required. The first thing to consider is an ideal porous material solid. In this study, the solid is represented as an isotropic rock with a uniformly elastic matrix and pores of various sizes and shapes, as noted by Zimmerman (1991). The change in its total volume is given by:

$$dV_b = -C_r V_b^i dP. \tag{A-1}$$

Considering that a uniform hydrostatic stress $\{dP_c\}$ is applied to the external surface and a uniform hydrostatic pressure $\{dP_p\}$ is applied to the internal surface, the stress system is represented as $\{dP_c, dP_p\}$. Now, assuming an increase in stress $\{dP, 0\}$, indicating changes in the confining pressure, this will lead to variations in the bulk volume, expressed as:

$$dV_b = -C_{bc} V_b^i dP. \tag{A-2}$$

Conversely, if an increase in stress $\{0, dP\}$ corresponding to variations in pore pressure is considered, the alterations in the bulk volume that will occur will be articulated as follows:

$$dV_b = C_{bp} V_b^i dP. \tag{A-3}$$

Given that these changes are infinitesimally small and applying the superposition principle, the deformations caused by the stress increment $\{0, dP\}$ will be equal to the difference in the resulting deformations between $\{dP, dP\}$ and $\{dP, 0\}$. Refer to **Fig. A - 1**, which results in:

$$C_{bp} V_b^i dP = -C_r V_b^i dP - \left(-C_{bc} V_b^i dP\right) = (C_{bc} - C_r) V_b^i dP. \tag{A-4}$$

Hence:

$$C_{bp} = C_{bc} - C_{r.} \tag{A-5}$$

Similarly, it is feasible to derive expressions that correlate the definitions of pore compressibility, denoted as C_{pc} and C_{pp}. Assuming once more an increase of stresses both within and outside the porous solid $\{dP, dP\}$, the resulting deformations are similarly summarized as follows:

$$C_{pp}V_p^i dP = -C_r V_p^i dP - \left(-C_{pc}V_p^i dP\right) = \left(C_{pc} - C_r\right)V_p^i dP. \tag{A-6}$$

This yields:

$$C_{pp} = C_{pc} - C_r. \tag{A-7}$$

Bulk and pore compressibilities can be related via the Maxwell-Betti reciprocal theorem of elasticity. This theorem states that when an elastic body is subjected to two sets of forces, denoted as F_1 and F_2, the work done by F_1 acting through the displacements due to F_2 is precisely equal to the work done by F_2acting through the displacements caused by F_1. Applying this theorem to the force sets $\{dP, 0\}$ and $\{0, dP\}$, the work done by the first set through the displacements induced by the second set is expressed as:

$$W^{12} = -dP[dV_b(0, dP)] = -dP\left(-C_{bp}V_b^i dP\right) = -C_{bp}V_b^i(dP)^2 \tag{A-8}$$

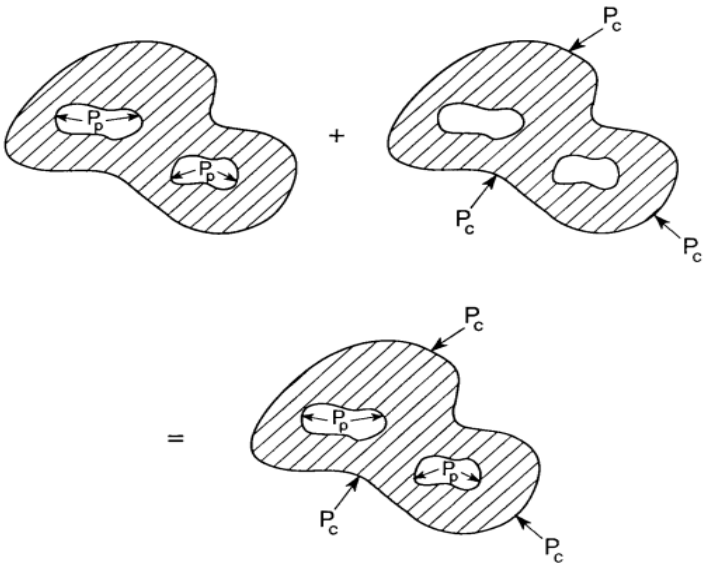

Fig. A - 1: Superposition principle used in the derivation of the relationships between the various compressibilities. (Zimmerman., 1991).

The negative sign is logical when recognizing that a positive confining pressure will oppose the unit normal vector outside the external surface. Conversely, the bulk volume increases if the displacement aligns with the unit normal vector. Likewise, W^{21} is expressed as follows:

$$W^{21} = dP\left[dV_p(dP, 0)\right] = dP\left(-C_{pc}V_p^i dP\right) = -C_{pc}V_p^i(dP)^2. \qquad \text{(A-9)}$$

In this case, contrary to the above, the negative sign is unnecessary because the pore pressure acts in the same direction as the increase in pore volume. The Maxwell-Betti reciprocal theorem of elasticity implies that $W^{12} = W^{21}$, so comparing **Eqs. A-8** and **A-9** yields $C_{bp}V_b^i = C_{pc}V_p^i$; using the definition of porosity $\phi = \frac{V_p}{V_b}$, the result is:

$$C_{bp} = \phi^i C_{pc}. \qquad \text{(A-10)}$$

This expression is valid only if it assumes elastic behavior; it does not require that the matrix be homogeneous or isotropic.

Equations **Eqs. A-5**, **A-7**, and **A-10** establishes three relationships among the four compressibilities $\{C_{pc}, C_{pp}, C_{bc}, C_{bp}\}$, using ϕ^i and C_r as the only explicit parameters. Therefore, the remaining three compressibilities can be defined in terms of $\{C_{bc}, C_r, \phi^i\}$ as follows:

$$C_{bp} = C_{bc} - C_r. \tag{A-11}$$

$$C_{pc} = (C_{bc} - Cr)/\phi^i. \tag{A-12}$$

$$C_{pp} = C_{bc} - (1 + \phi^i)C_r/\phi^i. \tag{A-13}$$

APPENDIX B

This appendix presents the literature about the elastic constants analyzed in this study. They were evaluated using the formulas established by Zoback (2007). While there are many expressions to calculate the elastic parameters, only two of these properties are essential and independent, allowing the inference of the others. Below is a description of each parameter discussed.

Bulk modulus

It is defined as the ratio of the change in applied stress to the change in volumetric strain caused, or more simply, as the inverse of total volumetric compressibility. It is denoted as:

$$K = \frac{\Delta P_c}{\Delta \varepsilon_v}. \tag{B-1}$$

In other words, it measures a material's resistance to uniform compression under hydrostatic stress conditions.

Young's modulus

Referred to as the modulus of elasticity, it is defined as the ratio of axial stress to axial strain, represented as:

$$E = \frac{\sigma}{\varepsilon}. \tag{B-2}$$

A higher E modulus value signifies greater rock stiffness, making deformation more challenging; in contrast, a lower E value suggests the rock is more deformable.

Poisson's ratio

As Jaeger et al. (2007) noted, Poisson's ratio refers to the negative ratio of transverse strain to longitudinal strain when subjected to uniaxial stress. It is represented by the symbol v and can be calculated using the following formula:

$$v = -\frac{\varepsilon_2}{\varepsilon_1} = -\frac{\varepsilon_3}{\varepsilon_1} \text{ or } v = \frac{\lambda}{2}(\lambda + G). \quad \text{(B-3)}$$

In sandstones, the usual range is 0.15 to 0.25. Simply put, Poisson's ratio measures the rock's compressibility in a direction perpendicular to the applied stress.

Shear modulus

The shear modulus measures a material's resistance to deformation from shear stresses, defined as the ratio of shear stress to the resulting deformation. The expression used in this paper is:

$$G = 3\left(K - \frac{\lambda}{2}\right). \quad \text{(B-4)}$$

Lamé constant

Traditionally, this is defined as the bulk modulus minus two-thirds of the shear modulus, expressed as follows:

$$\lambda = K - \frac{2}{3}G. \quad \text{(B-5)}$$

In conclusion, **Fig. B - 1** provides a summary of the elastic moduli along with various estimation methods.

K	E	λ	ν	G	M
$\lambda + \frac{2G}{3}$	$G\frac{3\lambda + 2G}{\lambda + G}$	–	$\frac{\lambda}{2(\lambda + G)}$	–	$\lambda + 2G$
–	$9K\frac{K - \lambda}{3K - \lambda}$	–	$\frac{\lambda}{3K - \lambda}$	$3\frac{K - \lambda}{2}$	$3K - 2\lambda$
–	$\frac{9K - G}{3K - G}$	$K - \frac{2G}{3}$	$\frac{3K - 2G}{2(3K + G)}$	–	$K + 4\frac{G}{3}$
$\frac{\varepsilon G}{3(3G - E)}$	–	$G\frac{E - 2G}{3G - E}$	$\frac{E}{2G} - 1$	–	$G\frac{4G - E}{3G - E}$
–	–	$3K\frac{3K - E}{9K - E}$	$\frac{3K - E}{6K}$	$\frac{3KE}{9K - E}$	$3K\frac{3K + E}{9K - E}$
$\lambda\frac{1 + \nu}{3\nu}$	$\lambda\frac{(1 + \nu)(1 - \nu)}{\nu}$	–	–	$\lambda\frac{1 - 2\nu}{2\nu}$	$\lambda\frac{1 - \nu}{\nu}$
$G\frac{2(1 + \nu)}{3(1 - 2\nu)}$	$2G(1 + \nu)$	$G\frac{2\nu}{1 - 2\nu}$	–	–	$G\frac{2 - 2\nu}{1 - 2\nu}$
–	$3K(1 - 2\nu)$	$3K\frac{\nu}{1 + \nu}$	–	$3K\frac{1 - 2\nu}{2 + 2\nu}$	$3K\frac{1 - \nu}{1 + \nu}$
$\frac{E}{3(1 - 2\nu)}$	–	$\frac{E\nu}{(1 + \nu)(1 - 2\nu)}$	–	$\frac{E}{2 + 2\nu}$	$\frac{E(1 - \nu)}{(1 + \nu)(1 - 2\nu)}$

Fig. B - 1: Relationship between elastic modulus for an isotropic material. (Zoback., 2007).